SN H0pe: The First Measurement of H_0 from a Multiply Imaged Type Ia Supernova, Discovered by JWST

Massimo Pascale[1] , Brenda L. Frye[2] , Justin D. R. Pierel[3] , Wenlei Chen[4] , Patrick L. Kelly[5] , Seth H. Cohen[6] ,
Rogier A. Windhorst[6] , Adam G. Riess[3,7] , Patrick S. Kamieneski[6] , José M. Diego[8] , Ashish K. Meena[9] ,
Sangjun Cha[10] , Masamune Oguri[11,12] , Adi Zitrin[9] , M. James Jee[10,13] , Nicholas Foo[6] , Reagen Leimbach[2] ,
Anton M. Koekemoer[3] , C. J. Conselice[14] , Liang Dai[15] , Ariel Goobar[16] , Matthew R. Siebert[3] , Lou Strolger[3] , and
S. P. Willner[17]

[1] Department of Astronomy, University of California, 501 Campbell Hall #3411, Berkeley, CA 94720, USA
[2] Department of Astronomy/Steward Observatory, University of Arizona, 933 N. Cherry Avenue, Tucson, AZ 85721, USA
[3] Space Telescope Science Institute, 3700 San Martin Drive, Baltimore, MD 21218, USA
[4] Department of Physics, Oklahoma State University, 145 Physical Sciences Bldg, Stillwater, OK 74078, USA
[5] Minnesota Institute for Astrophysics, University of Minnesota, Minneapolis, MN 55455, USA
[6] School of Earth and Space Exploration, Arizona State University, Tempe, AZ 85287-1404, USA
[7] Department of Physics and Astronomy, Johns Hopkins University, Baltimore, MD 21218, USA
[8] Instituto de Fisica de Cantabria (CSIC-C), Avda. Los Castros s/n, 39005 Santander, Spain
[9] Department of Physics, Ben-Gurion University of the Negev, P. O. Box 653, Be'er-Sheva 84105, Israel
[10] Department of Astronomy, Yonsei University, 50 Yonsei-ro, Seoul 03722, Republic of Korea
[11] Center for Frontier Science, Chiba University, Chiba 263-8522, Japan
[12] Department of Physics, Graduate School of Science, Chiba University, 1-33 Yayoi-Cho, Inage-Ku, Chiba 263-8522, Japan
[13] Department of Physics and Astronomy, University of California, Davis, One Shields Avenue, Davis, CA 95616, USA
[14] Jodrell Bank Centre for Astrophysics, Alan Turing Building, University of Manchester, Oxford Road, Manchester M13 9PL, UK
[15] Department of Physics, University of California, 366 Physics North MC 7300, Berkeley, CA 94720, USA
[16] The Oskar Klein Centre for Cosmoparticle Physics, Department of Physics, Stockholm University, SE-10691 Stockholm, Sweden
[17] Center for Astrophysics | Harvard & Smithsonian, 60 Garden Street, Cambridge, MA 02138, USA

Abstract

The first James Webb Space Telescope (JWST) Near InfraRed Camera imaging in the field of the galaxy cluster PLCK G165.7+67.0 ($z = 0.35$) uncovered a Type Ia supernova (SN Ia) at $z = 1.78$, called "SN H0pe." Three different images of this one SN were detected as a result of strong gravitational lensing, each one traversing a different path in spacetime, thereby inducing a relative delay in the arrival of each image. Follow-up JWST observations of all three SN images enabled photometric and rare spectroscopic measurements of the two relative time delays. Following strict blinding protocols which oversaw a live unblinding and regulated postunblinding changes, these two measured time delays were compared to the predictions of seven independently constructed cluster lens models to measure a value for the Hubble constant, $H_0 = 71.8 + 9.2 - 8.1$ km s^{-1} Mpc^{-1}. The range of admissible H_0 values predicted across the lens models limits further precision, reflecting the well-known degeneracies between lens model constraints and time delays. It has long been theorized that a way forward is to leverage a standard candle, but this has not been realized until now. For the first time, the lens models are evaluated by their agreement with the SN absolute magnifications, breaking degeneracies and producing our best estimate, $H_0 = 75.7^{+8.1}_{-5.5}$ km s^{-1} Mpc^{-1}. This is the first precise measurement of H_0 from a multiply imaged SN Ia and only the second from any multiply imaged SN.

1. Introduction

Determination of the current expansion rate of the Universe (the Hubble constant, H_0) across a wide range of redshifts provides a fundamental test of the standard cosmological model, Lambda cold dark matter (ΛCDM). While this model succeeds in reproducing an abundance of observed cosmological phenomena, disagreement between independent measurements of H_0 at early and late times in the Universe raises doubts about the model's reliability. This tension primarily results from two

independent precision methods for measuring H_0: Type Ia supernovae (SNe Ia) using the local-distance-ladder approach and cosmic microwave background (CMB) observations in conjunction with the ΛCDM model. Confirming or resolving the H_0 discrepancy is crucial for fundamental physics including the effects of neutrinos, the nature of dark energy, and the spatial curvature of the Universe.

For the local distance ladder, the Supernova H_0 for the Equation of State (SH0ES) team's (A. G. Riess et al. 2022) calibration of distances to nearby Cepheid variable stars in multiple ways, followed by calibration of SNe Ia which share host galaxies with Cepheids, yields $H_0 = 73.29 \pm 0.090$ km s^{-1} Mpc^{-1} (Y. S. Murakami et al. 2023). In contrast, CMB measurements (Planck Collaboration et al 2020) from the Planck satellite

favor $H_0 = 67.4 \pm 0.5 \, \mathrm{km \, s^{-1} \, Mpc^{-1}}$ assuming a flat ΛCDM cosmology. This apparent $>5\sigma$ disagreement between two premier methods is the basis of what is known as the "Hubble tension." Examining other independent H_0 measurements can delineate the underlying discrepancy. Local-distance-ladder measurements using Hubble Space Telescope (HST) imaging of the tip of the red giant branch stars (TRGBs) to calibrate SNe Ia from the Carnegie-Chicago Hubble Program (CCHP; W. L. Freedman et al. 2019), the Extragalactic Distance Database (EDD; G. S. Anand et al. 2022), and Comparative Analysis of TRGBs (CATs; D. Scolnic et al. 2023) yield a range in H_0 of 70–73 km s^{-1} Mpc^{-1}. Through comparison of measured colors to measured surface-brightness fluctuations (SBFs) calibrated on TRGBs and Cepheids, J. P. Blakeslee et al. (2021) found $H_0 = 73.3 \pm 0.7 \pm 2.4 \, \mathrm{km \, s^{-1}}$ Mpc^{-1}, while P. Garnavich et al. (2023) found $74.6 \pm 0.9 \pm 2.7 \, \mathrm{km \, s^{-1} \, Mpc^{-1}}$ by adding SNe Ia as the top rung. In a "single-rung" distance ladder, the Maser Cosmology Project (MCP; D. W. Pesce et al. 2020) combined six maser distances and peculiar velocities to find $H_0 = 73.9 \pm 3.0 \, \mathrm{km \, s^{-1} \, Mpc^{-1}}$. Another single-rung method uses time variability between the multiple images of strongly gravitationally lensed quasars. The Time Delay COSMOgraphy (TDCOSMO) collaboration leveraged a joint measurement across seven lensed quasars to find $H_0 = 74.2^{+1.6}_{-1.6} \, \mathrm{km \, s^{-1} \, Mpc^{-1}}$ assuming power-law mass profiles for the lens and a flat ΛCDM cosmology, and $H_0 = 73.3^{+5.8}_{-5.8} \, \mathrm{km \, s^{-1} \, Mpc^{-1}}$ using free-form mass profiles (A. J. Shajib et al. 2023; see also M. Millon et al. 2020, K. C. Wong et al. 2020; S. Birrer et al. 2020). This growing catalog of independent measurements has already provided insights into the Hubble tension (L. Verde et al. 2024), and new measurements at intermediate redshifts $1 < z < 10$ are imperative in elucidating when in cosmic history this discrepancy occurs.

S. Refsdal (1964) first recognized that strong gravitational lensing of SNe enables another independent method for measuring H_0. The "strong" regime of gravitational lensing refers to the deflection of the light of a distant background object (star, galaxy, or QSO) by a foreground galaxy or cluster of galaxies such that the image of a single object is observed at multiple positions on the sky. For each observed image of an "image system," the background object's light traverses a different path length, resulting in different travel times for photons to each image. Transient events within the lensed object (e.g., an SN or quasar variability) enable measurement of the time delay between multiple images. The time delay, together with a model of the lensing mass distribution, yields the timed delay distance to the source object, a quantity inversely proportional to H_0.

Although initially envisioned for SNe, inference of H_0 through strong-lensing (SL) time delays was first applied to multiply imaged quasars lensed by single foreground galaxies (S. H. Suyu & A. Halkola 2010). The technique, known as time-delay cosmography, was not realized for SNe until the discovery of "S. Refsdal," a multiply imaged Type II SN (SN II) found in the Massive Cluster Survey (MACS) J1149.6+2223 cluster field (P. L. Kelly et al. 2015). Crucially, SL SNe in galaxy-cluster lenses provide an independent route for measuring H_0 whose systematics are distinct from the distance-ladder, quasar time-delay cosmography, and CMB approaches (S. H. Suyu et al. 2024). SN Refsdal was observed as four multiple images in an Einstein cross around a single elliptical-galaxy lens (a "galaxy–galaxy" lens). A fifth image

with an $\sim$1 yr relative time delay was predicted (K. Sharon & T. L. Johnson 2015; M. Oguri 2015; J. M. Diego et al. 2016; C. Grillo et al. 2016; T. Treu et al. 2016) and later observed (P. L. Kelly et al. 2016). The relatively long time delay enabled SN Refsdal to be the first lensed SN for which meaningful constraints of H_0 could be inferred, and the nature of the galaxy-cluster-scale lens gave these constraints distinct systematics from previous galaxy–galaxy lens methods (C. Grillo et al. 2018; J. Vega-Ferrero et al. 2018). The constraints and their systematics were later quantified by C. Grillo et al. (2020). The most robust constraints to date from SN Refsdal were provided by P. L. Kelly et al. (2023), who inferred $H_0 = 64.8^{+4.4}_{-4.3} \, \mathrm{km \, s^{-1} \, Mpc^{-1}}$ or $H_0 = 66.6^{+4.1}_{-3.3} \, \mathrm{km \, s^{-1} \, Mpc^{-1}}$ depending on the set of lens models used. Y. Liu & M. Oguri (2024) and C. Grillo et al. (2024) further explored the systematics, employing lens modeling approaches designed explicitly for time-delay cosmography.

On the heels of the discovery of SN Refsdal, several other lensed supernova have been observed. These include other SNe II, such as the $z \sim 3$ SN in the A370 cluster field, which allowed detailed studied of shock cooling in a red supergiant SN (W. Chen et al. 2022), as well as the SN Ia "iPTF16geu" at $z = 0.409$ (A. Goobar et al. 2017), which was the first SN Ia to have multiple images observed. It was followed by "SN Requiem" at $z = 1.95$ (S. A. Rodney et al. 2021), and "SN Zwicky" at $z = 0.3554$ (A. Goobar et al. 2023; J. D. R. Pierel et al. 2023). Both iPTF16geu and SN Zwicky were galaxy-scale lenses, whose of order day-long time delays limited inference of H_0 to $\gtrsim$40% precision (S. Dhawan et al. 2020; J. D. R. Pierel et al. 2023). By contrast, the galaxy-cluster-scale lens of SN Requiem has a nearly decade-long time delay, which will yield a precise measurement of H_0 in 2037 when the SN counterimage is predicted to appear (S. A. Rodney et al. 2021). In the same host galaxy as SN Requiem, a second SN, "SN Encore," was discovered, marking the first occurrence of a lensed galaxy producing multiple observed SNe (J. D. R. Pierel et al. 2024). Across all of these SNe, SN Refsdal is the only one to provide precision H_0 constraints to date.

SN H0pe is a triply imaged SN Ia discovered in the galaxy-cluster field PLCK G165.7+67.0 (G165 hereafter, $z = 0.348$). It is a massive lensing galaxy cluster ($M_{\mathrm{tot}} = (2.6 \pm 0.3) \times 10^{14} \, M_\odot$; B. Frye et al. 2019; M. Pascale et al. 2022a), that induces a relatively long $\sim$100 day time delay between the first and third image, offering only the second-ever opportunity for precision SN time-delay cosmography and the first with an SN Ia. The three SN multiple images were discovered in James Webb Space Telescope (JWST)/Near InfraRed Camera (NIRCam) imaging in the lensed, near-infrared-bright host galaxy "Arc 2," which itself is triply imaged (B. Frye et al. 2023). M. Polletta et al. (2023) first measured the Arc 2 redshift as $z = 1.783 \pm 0.002$. The SN H0pe discovery paper (B. L. Frye et al. 2024) used follow-up JWST/NIRSpec spectroscopy to identify SN H0pe as an SN Ia, to confirm the SN host galaxy redshift to higher precision ($z = 1.7834 \pm 0.0005$), and to spectroscopically confirm a coincident galaxy overdensity at the redshift of SN H0pe. The known spectroscopic evolution of SNe Ia allowed W. Chen et al. (2024, in preparation) to determine the SN phases in the three multiple images of SN H0pe and thereby measure relative time delays of $-122.3^{+43.7}_{-43.8}$ days and $-49.3^{+12.2}_{-14.7}$ days between images a–b and c–b, respectively. Image b is the last to arrive and consequently shows the earliest phase of the SN, which was near

peak brightness at the time of discovery. This is the first time spectroscopy has provided useful time-delay constraints. W. Chen et al. (2024, in preparation) also classified SN H0pe as a normal SN Ia. J. D. R. Pierel et al. (2024, in preparation) used three epochs of JWST NIRCam six-band imaging to photometrically measure relative image time delays of $-116^{+10.8}_{-9.3}$ days and $-48.3^{+3.6}_{-4.0}$ days for images a–b and c–b, respectively.

Independently through the photometric and spectroscopic data sets respectively, J. D. R. Pierel et al. (2024, in preparation) and W. Chen et al. (2024, in preparation) use the standard-candle nature of the SN to constrain the absolute magnifications induced by SL. Absolute magnification measurements have long been thought to break degeneracies among mass models inherent in H_0 measurements from SL time delays (E. E. Falco et al. 1985; T. S. Kolatt & M. Bartelmann 1998; M. Oguri & Y. Kawano 2003; P. Schneider & D. Sluse 2013), yet have previously been unavailable for time-delay cosmography. For example in the case of the cluster-lensed SN Refsdal, the inferred H_0 was found to vary across 23 different lens mass models despite all satisfying the same lensing constraints. However, since H_0 was found to strongly correlate with the predicted magnifications, magnification measurements could have broken this degeneracy (Y. Liu & M. Oguri 2024). SN H0pe provides the first opportunity to harness the standard candle for time-delay cosmography.

This paper presents the first precise measurement of H_0 from time-delay cosmography of an SL SN Ia. The outline is as follows. Section 2 summarizes the underlying theory of time-delay cosmography. Section 3 describes the HST and JWST observations that led to SN H0pe's discovery and subsequent analysis. Sections 4 and 5 briefly summarize the photometric light-curve (LC) fitting and spectroscopic age-dating analyses. Section 6 details the construction of the seven contributing lens models. Section 7 outlines the process through which H_0 was derived from measured observables. Section 8 outlines the guidelines for the blinded inference. Section 9 presents the results of the H_0 inference. Section 10 discusses the unique advantages provided by the SN Ia, the robustness of the various inference approaches, and the overall error budget. Finally, Section 11 discusses future work and how SN H0pe fits into the broader picture of time-delay cosmography.

Throughout this analysis, we enforced a blinding between the seven independent lens models, the photometrically derived time delays, and the spectroscopically derived time delays from each other. Changes made after the unblinding and the impacts of each change are explicitly discussed in Section 8.

2. Time-delay Cosmography

Here we briefly outline how the time delay, $\Delta t_{i,j}$, between any two lensed images i and j of a multiply imaged source depends on the positions of the observed multiple images with respect to the source, the local lensing potential, and the assumed cosmological model. For an individual source at angular position β with a corresponding lensed image observed at angular position θ, the time delay can be expressed as:

$$t(\boldsymbol{\theta}, \boldsymbol{\beta}) = \frac{1 + z_l}{c} \frac{D_l D_s}{D_{ls}} \left[\frac{1}{2}(\boldsymbol{\theta} - \boldsymbol{\beta})^2 - \psi(\boldsymbol{\theta}) \right], \quad (1)$$

where z_l is the redshift of the lensing cluster, $\psi(\boldsymbol{\theta})$ is the lensing potential at the observed image position $\boldsymbol{\theta}$, and D_l, D_s, and D_{ls} are the angular diameter distances to the lens, the source, and

between the lens and source, respectively. If instead we measure the time delay between any two images of a set of multiple images:

$$\Delta t_{i,j}(\boldsymbol{\theta_i}, \boldsymbol{\theta_j}) = D_{\Delta t} \Delta \tau_{i,j}(\boldsymbol{\theta_i}, \boldsymbol{\theta_j}, \boldsymbol{\beta}), \quad (2)$$

where τ is the Fermat potential, with $\tau(\boldsymbol{\theta}, \boldsymbol{\beta}) = \frac{1}{2}(\boldsymbol{\theta} - \boldsymbol{\beta})^2 - \psi(\boldsymbol{\theta})$ (P. Schneider 1985; R. Blandford & R. Narayan 1986). $D_{\Delta t}$ is the so-called "time-delay distance," $D_{\Delta t} = \frac{1 + z_l}{c} \frac{D_l D_s}{D_{ls}}$, and is dependent on the angular diameter distances and hence the cosmological model (S. Refsdal 1964; P. Schneider et al. 1992; S. H. Suyu & A. Halkola 2010). $D_{\Delta t}$ is inversely proportional to H_0, while being only weakly dependent on other cosmological parameters (V. Bonvin et al. 2017). Hence, if the time delay between any two multiple images is known, as well as the redshifts of the lens and source, then a model of the lensing potential is necessary to constrain H_0.

In practice a lens model can be constructed from lensing observables, such as the observed positions of multiply imaged galaxies or information of the foreground lensing galaxies, and assumes a fiducial value of H_0, $H_0^{\rm fid} = 70$ km s^{-1} Mpc^{-1}, to predict a fiducial time delay $\Delta t_{i,j}^{\rm fid}$. Following Equation 1, the true measured time delay for any image pair can be related to this lens model fiducial time delay by rescaling H_0 while holding all other cosmological parameters fixed, in turn inferring H_0:

$$\Delta t_{i,j}^{\rm pred}(H_0) = \Delta t_{i,j}^{\rm fid} \times \frac{70 \quad {\rm km} \quad {\rm s}^{-1} \quad {\rm Mpc}^{-1}}{H_0}. \quad (3)$$

An alternative approach can be accomplished by using measured time delays as input lens model constraints and freely optimizing for all cosmological parameters (e.g., C. Grillo et al. 2020, 2024), which has the advantage of probing degeneracies between H_0 and other cosmological parameters under different cosmologies. However functionality for this was not available to all lens models in this work, and the use of the time delays as input constraints for the lens models would have conflicted with the blinding goals of this work, as multiple lens model teams had constructed G165 lens models prior to the discovery of SN H0pe. Additionally, this would have added time-delay ratio constraints to these models, which we instead reserved as a blinded prediction to be incorporated into the final weighting scheme (see Section 7). Finally, we point out that when imposing a standard flat ΛCDM cosmology, the lens model time delay is expected to vary $\lesssim$1% with respect to $\Omega_{\rm m}$ across a typical range $\Omega_{\rm m} \in [0.2, 0.4]$ for the redshift of SN H0pe. While it is possible to explore parameter degeneracies under other cosmologies through such an approach (e.g., open ΛCDM), this is outside the intended scope of this work.

3. Observations

The discovery paper for SN H0pe (B. L. Frye et al. 2024) supplied details regarding the JWST imaging and spectroscopic data sets. In brief, SN H0pe was initially discovered in NIRCam images from the PEARLS GTO program (PI: Windhorst, PID: 1176; R. A. Windhorst et al. 2023). The discovery images were taken on 2023 March 31 in eight filters. The SN was recognized by comparing the F150W PEARLS NIRCam imaging to WFC3/IR F160W HST images taken on 2016 May 30 (Figure 1). The discovery prompted a JWST disruptive Director's Discretionary Time (DDT) program,
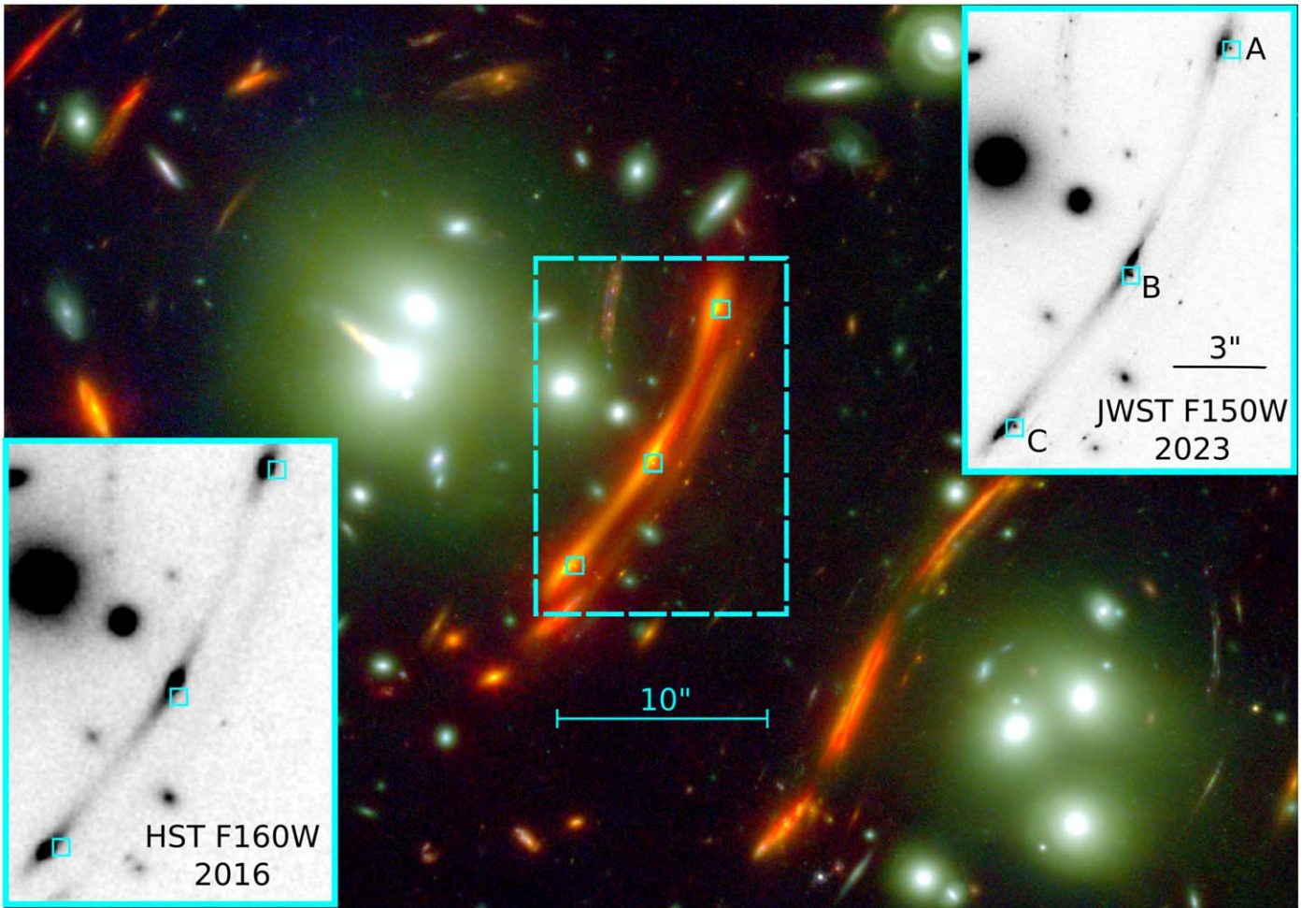
Figure 1. JWST/NIRCam color image in the central region of G165. Insets show a close-up view of the boxed region depicting the three multipole images of the host galaxy Arc 2 prior to SN H0pe in HST WFC3/IR F160W imaging from 2016 (lower left) and during its appearances in JWST/NIRCam F150W imaging from 2023 (upper right). The three images of the Type Ia SN H0pe appear only in the 2023 images, and their positions are marked by the blue boxes, where the "A," "B," and "C" refer to images a, b, and c, respectively. North is up and east is to the left.

which acquired two additional epochs of NIRCam imaging in six filters (PI: Frye, PID: 4446) on 2023 April 22 and May 9. Photometric analysis of the galaxy-cluster field was presented by B. L. Frye et al. (2024), and photometric LC fitting of the SN was presented by J. D. R. Pierel et al. (2024, in preparation).

The DDT program also acquired JWST/NIRSpec microshutter assembly (MSA) spectra (B. L. Frye et al. 2024; W. Chen et al. 2024, in preparation) in the PRISM, G140M, and G235M gratings targeting the SN host galaxy and the two brightest SN multiple images. The spectra, taken on April 22, confirmed the SN Ia type from the identification of the requisite blueshifted [Si II] $\lambda6355$ feature, Ca H and K, and other absorption-line features commonly found in SNe Ia (Figure 2).

4. Photometric Time Delays and Magnifications

The LC evolution of SNe Ia is well studied (e.g., E. Y. Hsiao et al. 2007; J. D. R. Pierel et al. 2021), such that precise measurements of the time delay can be made by fitting measured SN colors across multiepoch imaging. Given that there are three epochs of NIRCam imaging, and each epoch contains three SN multiple images, the SN evolution is photometrically sampled at nine points in time. Here we briefly summarize the LC fitting analysis of J. D. R. Pierel et al. (2024, in preparation). The halo of the bright galaxy host, a

significant source of noise, is reconstructed and subtracted through simultaneous fitting of its surface-brightness profile and cluster lens model with the GLEE software package (A. Halkola et al. 2006; S. H. Suyu & A. Halkola 2010; see details in G. B. Caminha et al. 2024, in preparation). The photometry of the SN multiple images is then fit simultaneously to BayeSN SN Ia models (K. S. Mandel et al. 2022; M. Grayling et al. 2024). Time delays are inferred by fitting a common set of LC parameters to each of the SN multiple images. The magnification ratios are estimated by normalizing the LC to image b, and then computing the ratios of images a and c relative to b. Finally, the absolute magnifications are estimated by comparing the peak F277W flux (approximately rest-frame Y band) predicted by the BayeSN models, to the population of field SNe Ia.

Statistical uncertainties of the inferred time delays and magnifications are estimated by bootstrapping the photometric uncertainties assuming Gaussian errors. Systematic uncertainties resulting from the BayeSN model itself are produced in a similar manner. Systematic uncertainties from chromatic microlensing are estimated by examining the range of fits to a set of 1000 simulated SN H0pe LCs with variable realizations of the foreground microlensing. Systematics from millilensing by dark matter subhalos in the foreground cluster lens are
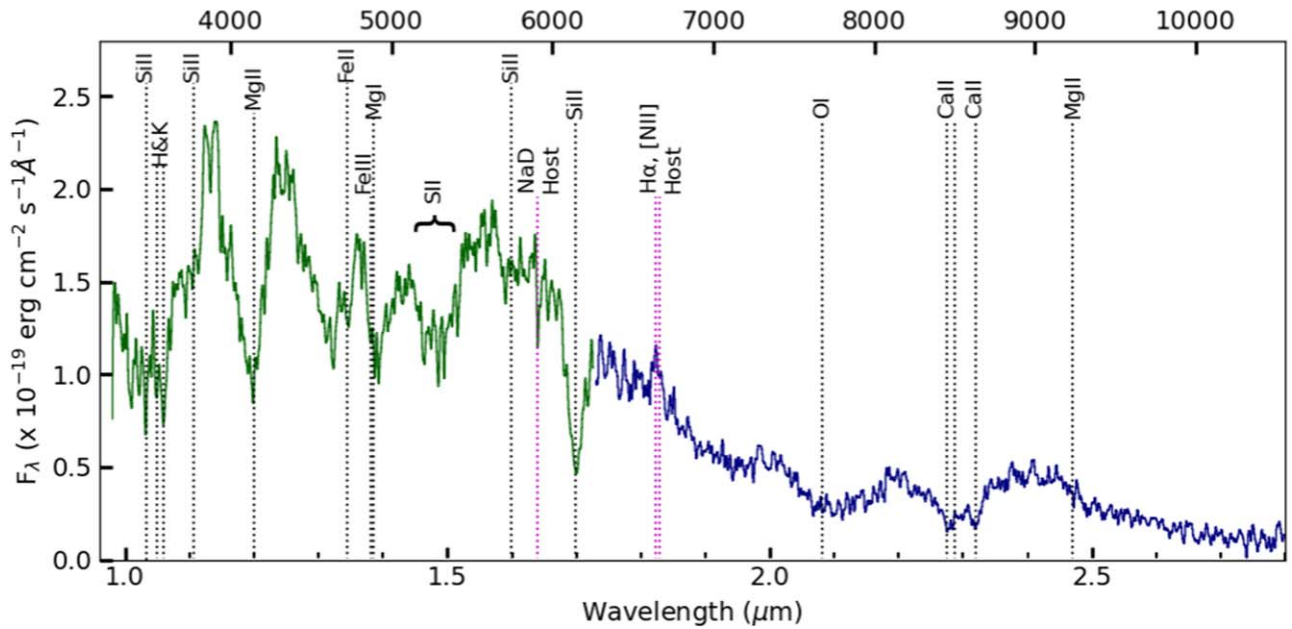
Figure 2. High signal-to-noise ratio NIRSpec spectrum of SN H0pe. The G140M (green) and G235M (blue) grating spectra are shown. Some prominent line features are identified, such as the [Si II] line blueshifted to rest-frame ~6150 Å that is a requisite line feature of an SN Ia. A few features are also traced to the SN host galaxy, such as Na D, Hα, and [N II] $\lambda\lambda$6548, 6584 (magenta dotted line). The observed wavelength is given on the lower abscissa and the rest wavelength in the frame of the host galaxy is provided on the upper abscissa.

achromatic, and applied directly as a correction to the distribution of inferred magnifications. Finally, the ~0.1 mag intrinsic scatter of SN Ia absolute magnitudes (D. M. Scolnic et al. 2018) is applied to the magnification distribution.

5. Spectroscopic Time Delays and Magnifications

Spectra from multiple images of an SL SN obtained during a single observing epoch enable the measurement of time delays via spectroscopic-based phase analysis. Previously, the lack of quality simultaneously obtained spectra have precluded such an analysis. Since SN H0pe was discovered from the PEARLS NIRCam Epoch 1 observation when its multiple images were near peak brightnesses, the rapid acquisition of spectra in a "disruptive" JWST DDT program using the JWST NIRSpec's MSA enabled the identification of the SN as Type Ia through the detection of the requisite blueshifted [Si II] λ6155 absorption-line feature.

The identification of SN H0pe as an SN Ia allowed for more straightforward template fitting to determine the phases between multiple images using spectroscopic methods. Below, we describe the process of measuring time delays through spectroscopic age dating from NIRSpec data. We refer to W. Chen et al. (2024, in preparation) for details.

Extraction of the SN spectrum from the NIRSpec data is performed using custom software designed to cope with background subtraction, host galaxy contamination, and bad pixels (e.g., cosmic rays). The error contribution from these potential systematics is included in the overall uncertainties, along with other sources of error such as slit loss and flux calibration. The relative delays between the multiple images' emitting times are estimated by determining their SN phases (days post-B-band peak brightness) through a joint Markov Chain Monte Carlo (MCMC) fit of the SN spectra against various spectroscopic templates (e.g., E. Y. Hsiao et al. 2007). The magnification is estimated by comparing the rest-frame Y-band magnitude of the best-fit spectral models with that of an unmagnified SN Ia at $z = 1.783$. Systematics from microlensing, millilensing, and the ~0.1 mag intrinsic scatter in SN Ia absolute magnitudes are addressed precisely as described in the photometric LC fitting section outlined previously.

6. Lens Modeling

To obtain the cluster lens model-predicted time delays and magnifications, seven different teams agreed to construct independent lens models for this analysis. All lens modelers were supplied with the same input constraints. These consist of 21 multiple-image systems (comprising 109 multiple images, 15 of which pertain to the SN and features within its host galaxy). Five multiple-image systems have spectroscopically confirmed redshifts, which corresponded to eight multiple images with spectroscopic data (1a, 1b, 1c, 2a, 2c, 5a, 8c, and 9c). The image-system and cluster-member catalogs are public (B. L. Frye et al. 2024).

The multiple-image systems were selected predominantly by eye based on similar colors and morphology and informed by spectroscopic, photometric, and lens-model-predicted redshift constraints. All lens modeling teams participated in the development and vetting of the image-system catalog, which was unanimously agreed upon.

Cluster members were determined via the 1.6 μm bump in color–color space from NIRCam photometry (M. Sawicki 2002). Candidates were additionally vetted through spectroscopic redshifts (where available) and a standard red-sequence cut (M. D. Gladders & H. K. C. Yee 2000). This cut removed two small galaxies situated near the SN host arc (R.A., decl. = 11:27:15.84, +42:28:32.41 and 11:27:15.62, +42:28:30.462). Photometric redshifts also indicate that these are in the background at $0.5 < z < 1$. Additionally, we identified a bright, early-type galaxy (R.A., decl. = 11:27:06.70, +42:27:50.46) in the NIRCam parallel field $> 2'$ from the apparent position of the SN host is in the foreground at $z \sim 0.28$. These galaxies were included in the catalog to the lens modelers to allow them to be optimized

separately from the cluster members (e.g., C. A. Raney et al. 2020; A. Acebron et al. 2022). NIRCam imaging with $m_{\rm lim} = 28$–29 (depending on filter) reveals no other galaxies that may contribute significant line-of-sight structure to the lens, but low-surface-brightness perturbers below the detection limit of the NIRCam images cannot be ruled out. The final catalog consisted of 161 cluster members, of which 21 were spectroscopically confirmed (following the criterion of M. Pascale et al. 2022a).

We emphasize that each lens model was created without knowledge of the photometric or spectroscopic time-delay and magnification measurements, and the results of any given model were also blinded from the other modeling teams. All lens models assume a fiducial flat cosmology $\Omega_{\rm m} = 0.3$, $\Omega_{\Lambda} = 0.7$, and $H_0^{\rm fid} = 70$ km s^{-1} Mpc^{-1}. The time delays and magnification predictions from the lens models are measured at the lens-model-predicted positions of the multiple images rather than the observed positions.

We briefly summarize the general methods of lens models included in this analysis, the assumptions made by each, and the expected systematics. A full discussion of each lens model can be found in Appendix A. The seven lens models in this analysis are broadly split into two categories. Parametric models (models 1, 2, and 3) assume the mass distribution is entirely characterized as the superposition of analytic mass density profiles. These models typically impose large-scale profiles to describe the cluster-scale dark matter halo, and smaller halos to describe each galaxy, which include priors based on the galaxy brightness or morphology (E. Jullo et al. 2007; M. Oguri 2010; A. Zitrin et al. 2015). Nonparametric models (models 4 and 6), on the other hand, make fewer assumptions on the profile of the cluster-scale dark matter, and allow a flexible grid to describe the mass distribution (J. M. Diego et al. 2005; I. Sendra et al. 2014). Some models (models 5 and 7) are so-called "semiparametric," and may make use of both analytic profiles and more flexible nonparametric distributions. Parametric models benefit from a small number of free parameters and mass distributions which more closely mirror the galaxy configuration of the cluster, while nonparametric methods are given greater freedom in the shape of the underlying mass distribution and include a number of regularization parameters and stopping criteria to avoid over-fitting and unphysical solutions (J. M. Diego et al. 2005; P. P. Ponente & J. M. Diego 2011; S. Cha & M. J. Jee 2022).

One of the contributing models, model 4, leverages weak gravitational lensing to construct their lens model (S. Cha et al. 2024). This applies shape distortions of background galaxies in the galaxy-cluster field as constraints on the cluster mass distribution, and extends far outside the locus of SL observables in the cluster center (e.g., N. Kaiser & G. Squires 1993; H. Hoekstra et al. 2000; M. Bradač et al. 2005; M. J. Jee et al. 2006). By incorporating weak lensing (WL) into SL models, it is possible to further constrain the steepness of the mass profile, which directly impacts the predicted time delay (M. Bradač et al. 2005; M. J. Jee et al. 2006; A. Zitrin et al. 2015).

Lens models may also differ in how they optimize to estimate their posteriors; that is, whether they minimize the separation of lensed multiple images traced back to the source plane or the separation of predicted and observed lensed multiple images in the image plane. The two approaches should in principle perform similarly (C. R. Keeton 2010), but source-plane optimization is generally much faster computationally. While there are concerns that source-plane optimization may be

less accurate than image-plane optimization in practice (e.g., C. R. Keeton 2001), SL modeling in the Frontier Fields era has shown that both produce quality lens models (e.g., M. Meneghetti et al. 2017). In the case of SN Refsdal, P. L. Kelly et al. (2023) successfully applied a sample consisting of both image- and source-plane optimization models infer H_0. This work similarly includes lens models which follow both approaches. We find the plane of optimization may in one modeling approach have a nonnegligible impact on the resulting time-delay and magnification posteriors, which is detailed in Appendix C. For the case of this model, the image-plane version was chosen over the source-plane version, as it was inherently more robust (see Section 8).

Lens model diversity broadly accounts for systematics regarding how the lensing mass and hence potential is parameterized. However, a number of systematics is expected to affect each lens model similarly. These include the thin-sheet mass assumption (E. E. Falco et al. 1985; S. Birrer et al. 2016), line-of-sight structure (N. Dalal et al. 2005; C. A. Raney et al. 2020; A. Acebron et al. 2022), multiplane lensing (C. McCully et al. 2014), millilensing from dark matter subhalos (L. Dai et al. 2020; D. Gilman et al. 2020), and the effects of large-scale structure not captured within the field of view (K. C. Wong et al. 2011).

Beyond providing a uniform set of lensing inputs, a number of decisions were left up to the expertise of each individual team (e.g., the plane of optimization, uncertainty of the lensed-image positions, and priors on the fitted parameters describing the analytic mass profiles). This reflects the realistic diversity of lens models in published works (e.g., M. Meneghetti et al. 2017; P. L. Kelly et al. 2023). While SN H0pe presents a valuable opportunity to explore lens modeling systematics, as is done in Appendix F, an exhaustive investigation of the full suite of lens modeling decisions is beyond the scope of this work.

7. Inferring H_0 through Bayesian Analysis

We followed a Bayesian approach to constrain H_0 similar to the case of SN Refsdal in P. L. Kelly et al. (2023). For any individual lens model, H_0 can be inferred by rescaling the lens-model-predicted time delays to match the photometrically and/or spectroscopically measured time delays. There are two measured time delays, $\Delta t_{\rm a,b}$ and $\Delta t_{\rm c,b}$ for the images a–b and images c–b, respectively. We can infer H_0 from both time delays simultaneously, which is advantageous compared to doing so separately because the time delays may be covariant with one another.

7.1. From Time Delays Alone

We begin with a minimal set of observables made up of only the two time delays $\mathcal{O}$: $\{\Delta t_{\rm a,b}, \Delta t_{\rm c,b}\}$, however this may be expanded to include other observables covariant with the time delays. For simplicity, we first consider only the photometric results. The goal is to determine the probability of H_0 given the observed LC $P(H_0|{\rm LC})$, and marginalize over each lens model $M_{\rm l}$. The LC yields measurements of each observable in $\mathcal{O}$, while each lens model $M_{\rm l}$ makes predictions for the same observables assuming the fiducial H_0. For each model, the fiducial H_0 is rescaled such that the model predictions best match the measurements from the LC. Using Bayes' theorem, we can write the probability for the value of H_0 from a single

lens model as:

$$p_m(H_0|\text{LC}) \propto P(H_0)P(M_1)\int P(\mathcal{O}|M_1; H_0)$$
$$\times\ P(\mathcal{O}|\text{LC})d\mathcal{O}_1...d\mathcal{O}_n, \qquad (4)$$

where n is the number of observables. Assuming the systematics of the lens models are not fully independent from one another, the overall likelihood is the weighted sum of the individual model likelihoods:

$$P(H_0|\text{LC}) = P(H_0)\sum_1^N\int P(\mathcal{O}|M_1; H_0)$$
$$\times\ P(\mathcal{O}|\text{LC})d\mathcal{O}_1...d\mathcal{O}_n, \qquad (5)$$

where N is the number of lens models. This formalism can be understood as enforcing two priors: (1) following Equation (4) each individual lens model will prefer values of H_0 that allow the lens model to best reproduce $\mathcal{O}$, and (2) following Equation (5) the lens models which best reproduce the observables will have the greatest weight in the sum and hence hold the most influence over the H_0 inferred across all lens models. For a set of observables containing only the two time delays, this implies that (1) each lens model will favor values of H_0 for which the model-predicted time delays (rescaled following Equation (3)) best match the two measured time delays and (2) the lens models which best match the ratio of the two time delays are the models which effectively determine the inferred H_0.

7.2. Including Absolute Magnifications

Constraints on any observables which are correlated with the time delays effectively translate into constraints on the time delays themselves. The SN absolute magnifications are found to correlate with the time delays in the lens models, and, by including them into $\mathcal{O}$, it is possible to infer H_0 to greater accuracy and precision than with time delays alone. The addition of the image a, b, and c absolute magnifications (μ) increases the total number of observables to five:

$$\mathcal{O}: \{\Delta t_{a,b},\ \Delta t_{c,b},\ \mu_a,\ \mu_b,\ \mu_c\}. \qquad (6)$$

The measurements for these observables are shown in Figure 3 and Table 1. Once again following the formalism of Equations (4) and (5), the lens model time-delay–magnification covariance implies that inducting magnification into $\mathcal{O}$ affects the H_0 inferred by each individual lens model, as well as the H_0 inferred across all lens models. Because the absolute magnification was unavailable for the Type II SN Refsdal, this marks the first case where it can be meaningfully leveraged for time-delay cosmography. We refer to Sections 10.1 and 10.2 for further discussion.

7.3. Including Spectroscopic Constraints

The spectroscopic data set yields measurements of all five observables independently from the photometric data set. Though the spectroscopic measurements are somewhat less precise, it is possible to constrain the observables to even greater precision through a joint-fitting approach. Assuming the spectroscopic and photometric constraints are fully independent, the likelihood of Equation (5) can be modified to include the spectroscopic measurements, such that we determine the probability of H_0 given both the observed LC, and the observed spectroscopic ("SP") evolution:

$$P(H_0|\text{LC, SP}) = P(H_0)\sum_1^N\int P(\mathcal{O}|M_1; H_0)P(\mathcal{O}|\text{LC})$$
$$\times\ P(\mathcal{O}|\text{Sp})d\mathcal{O}_1...d\mathcal{O}_n. \qquad (7)$$

Here $P(\mathcal{O}|\text{LC})$ and $P(\mathcal{O}|\text{Sp})$ refer to the posteriors for the photometric and spectroscopic constraints, respectively.

Altogether, we employ three approaches to the inference of H_0 following this formalism. First, we infer $H_{0,\text{TD-only}}$, which uses only the photometric constraints following Equation (5), and uses only the two time delays in the set of observables, $\mathcal{O}: \{\Delta t_{a,b},\ \Delta t_{c,b}\}$. For the second approach, we similarly follow Equation (5) with only photometric constraints, but include absolute magnifications, following the full set of observables given in Equation (6) to infer $H_{0,\text{phot-only}}$. Finally in the third approach, we follow Equation (7) to infer $H_{0,\text{phot + spec}}$, which includes all available constraints from photometry and spectroscopy. We note that $H_{0,\text{TD-only}}$ inference provided identical results when spectroscopic constraints are added, and hence we do not include it as a separate approach. Across all approaches, we assign a top-hat prior for the Hubble constant: $H_0 \in (30, 130)\ \text{km s}^{-1}\ \text{Mpc}^{-1}$. The parameterization of $P(\mathcal{O}|M_1; H_0)$, $P(\mathcal{O}|\text{LC})$, and $P(\mathcal{O}|\text{SP})$ from the lens model, LC fitting, and spectroscopic age-dating posteriors, respectively, as well as the integration of the likelihood, are described in Appendix D.

8. Blinded Analysis

8.1. Blinding Protocols

Blinding protocols were installed to reduce the impact of human bias. They established the information that could be shared between subgroups of our team, the live unblinding process, and the rules for which changes were allowable postunblinding. The values of the time delays and the implied magnifications from both LC analysis and spectroscopic analysis were not revealed to one another, nor to any of the lens modeling teams. The modelers assembled regularly to agree upon the set lensing constraints, such as the catalogs of lensed-image positions, spectroscopic redshifts, and photometry of the cluster galaxies as stated explicitly in B. L. Frye et al. (2024), and then constructed the individual lens models independently. All lens models submitted prior to unblinding were required to be included in the inference. More specifically, for the blinded inference of H_0, the relative time delays and absolute magnifications from photometry and spectroscopy were blinded via a median subtraction of the probability distribution function (PDF) of each measurement. One exception is that the spectroscopic time-delay and magnification measurements were unblinded to the lens model 5 predictions. This is because the spectroscopic measurements and the lens model construction were performed by the same team; however, the lens model was completed and locked prior to obtaining the spectroscopic results, and hence was blinded from the spectroscopic time delays and the magnifications.

The photometric and spectroscopic analysis timelines were different. To accommodate the staggered timelines, the initial live unblinding was performed only for $H_{0,\text{phot-only}}$, which the spectroscopic analysis remained blinded to until the $H_{0,\text{phot + spec}}$ value was unblinded at a later date. Postunblinding changes were only allowed to address errors. We defined an error to be a genuine mistake for which there is an objectively
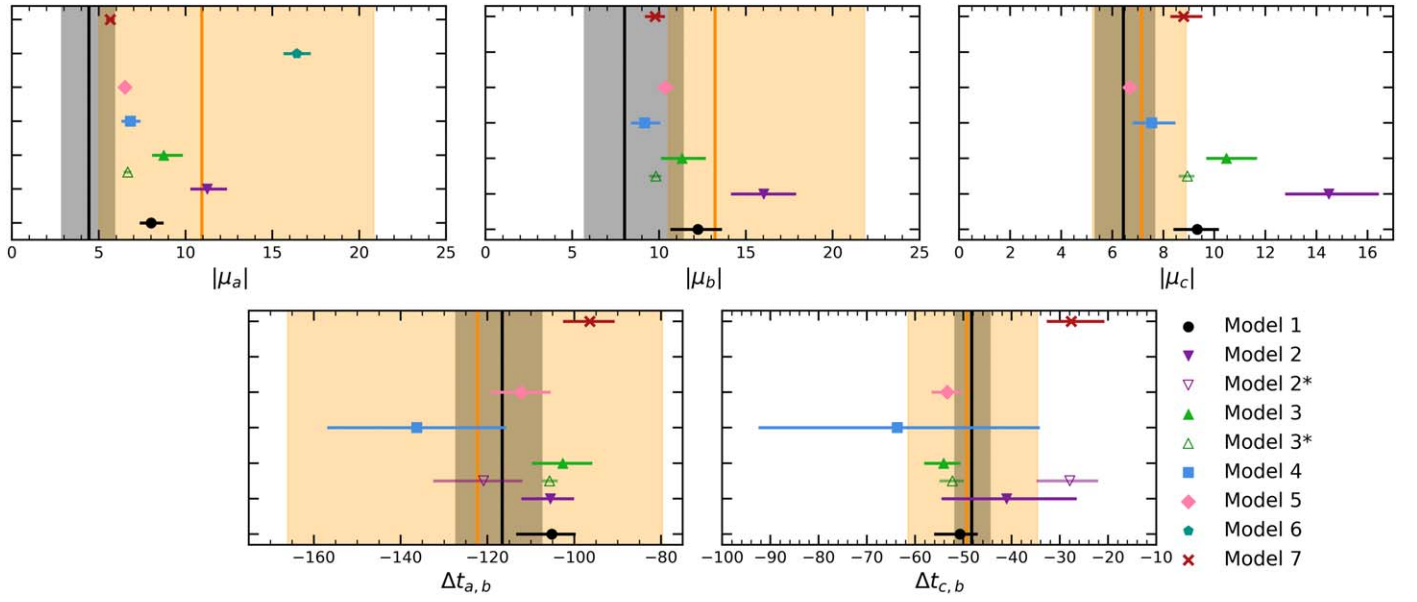
Figure 3. The absolute magnifications and relative time delays predicted by each of the seven contributing lens models (markers) and the measured quantities from photometric LC fitting (vertical black lines and gray swaths represent the median and 68% confidence interval, respectively) and spectroscopic age dating (orange lines and swaths). The x-axis limits are set for clarity, which omits model 6 for some quantities due to its inconsistency with both the other lens models and observations. The empty purple and green markers of "Model 2*" and "Model 3*" respectively represent the blinded results from models 2 and 3, which contained errors which were amended after unblinding (see Section 8). The lens-model-predicted time delays assume a fiducial $H_0 = 70$ km s^{-1} Mpc^{-1}. Following Equation (3), the time delays are inversely proportional to H_0, and rescaled for a range of values of H_0 to infer the total probability distribution.

correct solution rather than a subjective choice. Following the $H_{0,\text{phot-only}}$ unblinding, six errors were identified by this definition and corrected. Amending these errors ultimately resulted in an $\sim 1\sigma$ decrease in $H_{0,\text{phot-only}}$. While the resolution of these errors impacts the inference of H_0, the methodology was unchanged, and the details of each error and its impact on both the observables and the inferred H_0 are listed below.

8.2. Errors Corrected Postunblinding

Here we discuss the initial unblinded value of H_0, the seven errors found subsequent to the unblinding, and how amending the errors affected the inference. These errors result from genuine mistakes which had objective fixes. The following events are stated in chronological order beginning with the unblinding event. The initial unblinding was conducted using only photometric constraints, and all errors were found while blinded to the spectroscopic results. Hence, all values given pertain to $H_{0,\text{phot-only}}$.

The inference of $H_{0,\text{phot-only}}$ was unblinded live by revealing the median values of the distribution of measured magnifications and time delays from LC fitting, which yielded $H_{0,\text{phot-only}} = 81.3^{+15.9}_{-8.5}$ km s^{-1} Mpc^{-1}.

Postunblinding, the first error was a miscommunication between the LC fitting team and the team performing the H_0 inference that resulted in the exclusion of both the ~ 0.1 mag intrinsic scatter of SN Ia magnitudes and the scatter due to millilensing from the inference. Applying these effects broadened the measured magnification uncertainties by $\sim 25\%$, which resulted in an updated value of $H_{0,\text{phot-only}} = 79.6^{+15.0}_{-8.7}$ km s^{-1} Mpc^{-1}.

Second, the LC fitting team found an error in the simulations which estimate the systematic uncertainty due to microlensing. The uncertainties were based on the bias and standard deviation for distributions of measured magnifications relative to the simulated magnifications. However, the measured magnifications

were recorded as simply the ratio of measured amplitudes, which ignores the additional uncertainty from other LC parameters. This was updated to match the final method used to measure the true magnifications (see J. D. R. Pierel et al. 2024, in preparation, for details), which takes the full uncertainty into account. This further increased magnification uncertainties on images a and b by $\sim 10\%$–20% while image c remained mostly unaffected because of its phase at the second IR maximum. The same simulations were found to be using a different version of the BayeSN model (K. S. Mandel et al. 2022) for simulations and fitting, which led to an artificial bias in the fitted parameters. Fixing this error decreased the uncertainty of both time delays by $\sim 20\%$, altogether resulting in an updated value of $H_{0,\text{phot-only}} = 76.9^{+14.2}_{-8.2}$ km s^{-1} Mpc^{-1}.

Third, the LC fitting team discovered a numerical error in the removal of bias induced by systematics on the magnification and time delays. The median of each retrieved magnification and time-delay distribution, created from the simulations discussed above (and see J. D. R. Pierel et al. 2024, in preparation, for more details) was removed from the measured values to account for biases identified by fitting the simulations (following P. L. Kelly et al. 2023). After unblinding, it was discovered that this bias was being removed with a sign error. This shifted the median magnifications by $\lesssim 5\%$, the median $\Delta t_{c,b}$ by $\sim 4\%$, and $\Delta t_{a,b}$ by $\lesssim 1\%$. These resulted in an updated value of $H_{0,\text{phot-only}} = 75.9^{+15}_{-8.4}$ km s^{-1} Mpc^{-1}.

Fourth, the lens modeling team for model 3 corrected an error in the sampling of the lens model results, which had been used for estimation of the posterior distribution in the inference. This was caught serendipitously when the lens modeling team was requested to generate samples for other lens model parameters to gauge the dominant source of lens model uncertainty. The improper sampling resulted in a loss of covariance information between the magnification and time delays and significantly overestimated the time-delay

Table 1
Magnifications and Time Delays from the Cluster Lens Models, Photometry, and Spectroscopy

#	Lens Model	$\Delta t_{a,b}$	$\Delta t_{c,b}$	$|\mu_a|$	$|\mu_b|$	$|\mu_c|$
1	GLAFIC (M. Oguri 2010, 2021)	$-105.18^{+5.16}_{-7.89}$	$-50.71^{+3.37}_{-5.09}$	$8.02^{+0.64}_{-0.57}$	$12.23^{+1.30}_{-1.51}$	$9.32^{+0.80}_{-0.87}$
2	Zitrin-analytic[b] (A. Zitrin et al. 2015)	$-105.52^{+5.09}_{-6.32}$	$-41.06^{+14.27}_{-13.19}$	$11.25^{+1.05}_{-0.90}$	$16.03^{+1.77}_{-1.81}$	$14.48^{+1.91}_{-1.65}$
3[c]	LENSTOOL (J.-P. Kneib et al. 2011)	$-102.68^{+6.47}_{-6.80}$	$-54.09^{+3.18}_{-3.76}$	$8.75^{+1.01}_{-0.60}$	$11.32^{+1.29}_{-1.14}$	$10.47^{+1.14}_{-0.74}$
4	MARS (S. Cha & M. J. Jee 2022)	$-136.27^{+20.23}_{-20.32}$	$-63.72^{+29.24}_{-28.46}$	$6.82^{+0.50}_{-0.44}$	$9.17^{+0.80}_{-0.72}$	$7.55^{+0.86}_{-0.70}$
5	W. Chen et al. (2020)	$-112.25^{+6.43}_{-6.57}$	$-53.35^{+2.71}_{-2.99}$	$6.52^{+0.24}_{-0.22}$	$10.35^{+0.46}_{-0.41}$	$6.68^{+0.86}_{-0.22}$
6	WSLAP+ (J. M. Diego et al. 2005)	$-273.35^{+95.30}_{-95.30}$	$342.75^{+92.54}_{-92.54}$	$16.38^{+0.71}_{-0.71}$	$47.54^{+3.23}_{-3.23}$	$33.35^{+0.74}_{-0.74}$
7	Zitrin-LTM (A. Zitrin et al. 2009)	$-96.45^{+5.41}_{-5.85}$	$-27.64^{+6.52}_{-4.80}$	$5.66^{+0.15}_{-0.14}$	$9.77^{+0.47}_{-0.51}$	$8.80^{+0.67}_{-0.46}$
Photometry	J. D. R. Pierel et al. (2024, in preparation)[a]	$-116.60^{+10.83}_{-9.29}$	$-48.30^{+3.58}_{-3.97}$	$4.43^{+1.52}_{-1.60}$	$8.00^{+3.42}_{-2.34}$	$6.43^{+1.25}_{-1.13}$
Spectroscopy	W. Chen et al. (2024, in preparation)[a]	$-122^{+43.7}_{-43.8}$	$-49.3^{+12.2}_{-14.7}$	$10.93^{+8.63}_{-5.16}$	$13.22^{+7.49}_{-2.33}$	$7.14^{+1.53}_{-1.66}$

Notes. Top: the seven contributing cluster lens models, their primary references, and predicted time delays (in days) and magnifications given as the 68% confidence interval. Bottom: measurements of the corresponding quantities from photometry and spectroscopy.

[a] Values cited in this table assume Gaussian process regression interpolation for inference of the unlensed SN apparent magnitude.

[b] Time-delay values for this model were corrected for an error following unblinding. The error was in the time-delay measurement and did not require a modification of the underlying blind model. The initial blinded values were $\Delta t_{a,b} = -120.89^{+8.61}_{-11.31}$ days and $\Delta t_{c,b} = -27.94^{+5.56}_{-6.60}$ days. Details on the error and its correction are given in Section 8.

[c] This model was updated following unblinding. The blinded model values were $\Delta t_{a,b} = -105.68^{+1.51}_{-1.48}$ days, $\Delta t_{c,b} = -52.27^{+2.06}_{-2.44}$ days, $|\mu_a| = 6.67^{+0.11}_{-0.14}$, $|\mu_b| = 9.82^{+0.23}_{-0.31}$, and $|\mu_c| = 8.94^{+0.21}_{-0.29}$. Details on the blinded model and its correction are given in Section 8 and the model 3 section of Appendix A.

uncertainties by a factor of ~5. Re-generating the samples correctly did not require any changes in the lens model itself and did not change the median predictions of the magnifications or time delays. The lens model was given similar weight in the $H_{0,\text{phot-only}}$ inference both before and after making this adjustment, resulting in an updated value of $H_{0,\text{phot-only}} = 76.7^{+15.5}_{-6.7}$ km s^{-1} Mpc^{-1}.

Fifth, the lens modeling team for model 2 found an error in the calculation of the time delay from the lens model, where the source position sampled was offset by 1 pixel (0″03) in the source plane. This did not require any modification of the underlying lens model, only a change in how time delays were measured from it. As this significantly changed the time-delay distribution for this model, both the blinded values and the error-corrected values are shown Table 1 and Figure 3. Both $H_{0,\text{phot-only}}$ and $H_{0,\text{phot + spec}}$ were unaffected by this change as a result of negligible weighting both before and after the correction. For $H_{0,\text{TD-only}}$, however, the model weighting rose from ~0 to ~16%, changing the inference from $H_{0,\text{TD-only}} = 73.2^{+10.5}_{-6.4}$ km s^{-1} Mpc^{-1} to $H_{0,\text{TD-only}} = 71.8$ $71.8^{+9.2}_{-8.1}$ km s^{-1} Mpc^{-1}.

Sixth, during the review process it was determined that lens model 3 included two choices of model parameters which were not sufficiently justified, and ultimately the lens modeling teams mutually agreed these decisions were inappropriate. This specifically referred to the choice of positional uncertainty (0″03), which was found to be too small compared to prescriptions in the literature (e.g., T. L. Johnson et al. 2014; C. Grillo et al. 2016), and the choice to fix the cluster-member reference cutoff radii and velocity dispersions, which were found to bias the results. Updating the model with a more appropriate positional uncertainty of (0″3) and allowing the cluster-member parameters to be freely optimized was found to increase the time-delay and magnification fractional uncertainties as much as a factor of 5, and also increased the median magnifications by ~25%. The model updates are given in greater detail in Appendix A. We note that the model was also changed from source-plane to image-plane optimization, as the source-plane model had produced unphysical results at the larger positional uncertainty. Both $H_{0,\text{TD-only}}$ and $H_{0,\text{phot + spec}}$ were negligibly affected by this change, however in the $H_{0,\text{phot-only}}$ inference the model weighting decreased from 28% to 6%,

resulting in a change from $H_{0,\text{phot-only}} = 74.4^{+13.0}_{-6.0}$ km s^{-1} Mpc^{-1} to $H_{0,\text{phot-only}} = 76.7^{+15.5}_{-6.7}$ km s^{-1} Mpc^{-1}.

Seventh, it was found during the review process that the model 6 magnifications and time delays were measured at the observed SN positions rather than the model-predicted positions, which was inconsistent with the guidelines determined for lens model submission. To ensure a consistent approach across all models, the model 6 results were updated to instead use measurements made at the model-predicted positions. This did not involve any modification of the model itself, nor did this meaningfully affect the H_0 inference.

9. Results

Following the most straightforward approach, we inferred H_0 using only the photometric time delays, yielding $H_{0,\text{TD-only}} = 71.8^{+9.2}_{-8.1}$ km s^{-1} Mpc^{-1}. In this approach, the lens models are weighted based on their ability to reproduce the ratio between the two photometrically measured time delays. This inference is dominated by five models: model 5 (30%), model 1 (23%), model 2 (17%), model 4 (16%), and model 3 (9%). We found that including the spectroscopic time delays did not change the result due to their agreement with the photometric time delays while carrying uncertainties that were larger by a factor of ~4. Model 6 in particular is truncated by the 130 km s^{-1} Mpc^{-1} upper bound of the top-hat H_0 prior, resulting in only 3% of the weighting. Removal of this prior results in a dominant weighting of ~20% for $H_{0,\text{TD-only}}$, while the magnification-weighted approaches remain unaffected.

We next included magnification into the suite of observables, which yields $H_{0,\text{phot-only}} = 76.7^{+15.5}_{-6.7}$ km s^{-1} Mpc^{-1} from photometric constraints. Because the lens-model-predicted time delays and magnifications are correlated, the magnifications influence both the H_0 inferred by an individual lens model, as well as the relative weighting each model receives in the H_0 inferred across lens models. The weighting is such that the models which best reproduce the two measured time delays and three measured absolute magnifications simultaneously are given greater contribution to the PDF of $H_{0,\text{phot-only}}$. The result is primarily influenced by three lens models: model 5 is given

Table 2
H_0 Inferences

Lens Model	$H_{0,\text{phot + spec}}$	$H_{0,\text{phot-only}}$	$H_{0,\text{TD-only}}$	Weight$_{\text{phot + spec}}$	Weight$_{\text{phot-only}}$	Weight$_{\text{TD-only}}$
1	$76.05^{+6.41}_{-6.01}$	$75.55^{+6.71}_{-6.31}$	$69.74^{+7.11}_{-5.71}$	0.19	0.21	0.23
2	$83.55^{+6.61}_{-5.91}$	$82.05^{+7.01}_{-6.11}$	$64.73^{+7.31}_{-6.31}$	0.00	0.00	0.17
3	$76.05^{+5.51}_{-5.11}$	$75.85^{+5.91}_{-5.31}$	$72.24^{+6.21}_{-5.51}$	0.00	0.06	0.09
4	$93.96^{+15.02}_{-14.31}$	$93.66^{+14.91}_{-14.21}$	$85.96^{+16.02}_{-14.21}$	0.15	0.29	0.16
5	$74.54^{+5.11}_{-4.70}$	$73.84^{+5.31}_{-4.80}$	$73.84^{+5.51}_{-5.01}$	0.65	0.43	0.30
6	>130	>130	>130	0.00	0.00	0.00
7	$53.92^{+4.90}_{-4.40}$	$57.03^{+5.01}_{-4.50}$	$54.82^{+5.31}_{-4.80}$	0.00	0.01	0.03
Total	$75.7^{+8.1}_{-5.5}$	$76.7^{+15.5}_{-6.7}$	$71.8^{+9.2}_{-8.1}$	1.00	1.00	1.00

Note. The seven contributing cluster lens models with their individual predictions for the three H_0 (units of km s^{-1} Mpc^{-1}) inferences. Also listed are the relative weightings for each model in the likelihood across the three inferences. We also present the results for the total inference resulting from Equations (5) and (7).

43% of the weighting, model 4 is given 29%, and model 1 is given 21%. No single model dominates the inference, instead the three subdominant contributions individually predict different H_0 values, which ultimately broaden the resulting PDF.

Finally, we obtained the highest precision estimate by making use of all available constraints, inferring $H_{0,\text{phot+spec}} = 75.7^{+8.1}_{-5.5}$ km s^{-1} Mpc^{-1} from joint photometric–spectroscopic constraints. This inference is dominated by model 5 (65% of the weighting), with subdominant contributions by model 1 (19%) and model 4 (14%). While the individual lens model predictions are similar to those in $H_{0,\text{phot-only}}$ (that is, the joint time-delay constraints are effectively the same as those from photometry alone), the joint magnification constraints favor a single model, resulting in a significantly reduced uncertainty. For each approach, the H_0 predictions of each individual model as well as their assigned weights are shown in Table 2. These results are also illustrated in Figure 4, which shows the PDF of each lens model as well as the total PDF of H_0.

Figure 5 compares H_0 inferred from SN H0pe to other H_0 measurements, including that from SN Refsdal. The combined photometric–spectroscopic inference, $H_{0,\text{phot + spec}}$, provides the strongest constraints and agrees with most other late-time measurements, showing less than $<1\sigma$ tension with measurements from SH0ES, CCHP, and TDCOSMO (Y. S. Murakami et al. 2023; W. L. Freedman et al. 2019; K. C. Wong et al. 2020). By contrast, SN H0pe's $P(H_0 < 67.5\text{kms}^{-1}\ \text{Mpc}^{-1}) < 7\%$ shows 1.4–1.5σ tension with early time measurements. SN H0pe's H_0 is also in 1.3–1.5σ tension with the SN Refsdal result of P. L. Kelly et al. (2023). However, further exploration of SN Refsdal's systematics (Y. Liu & M. Oguri 2024; C. Grillo et al. 2024) measured $H_0 = 70.0^{+4.7}_{-4.9}$ km s^{-1} Mpc^{-1} and $H_0 = 65.1^{+3.5}_{-3.4}$ km s^{-1} Mpc^{-1}. The C. Grillo et al. (2024) result did not include priors from other cosmological experiments, while this work, P. L. Kelly et al. (2023), and Y. Liu & M. Oguri (2024) all assumed a flat ΛCDM cosmology.

10. Discussion

In this section, we discuss the implications of our results. Specifically, we highlight the impact of the constraints provided by Type Ia, evaluate systematics which may be present both in the measured magnification and the lens model predictions, and compute the relative error contributions between the photometric light curve fitting, spectroscopic age dating, and the lens models.
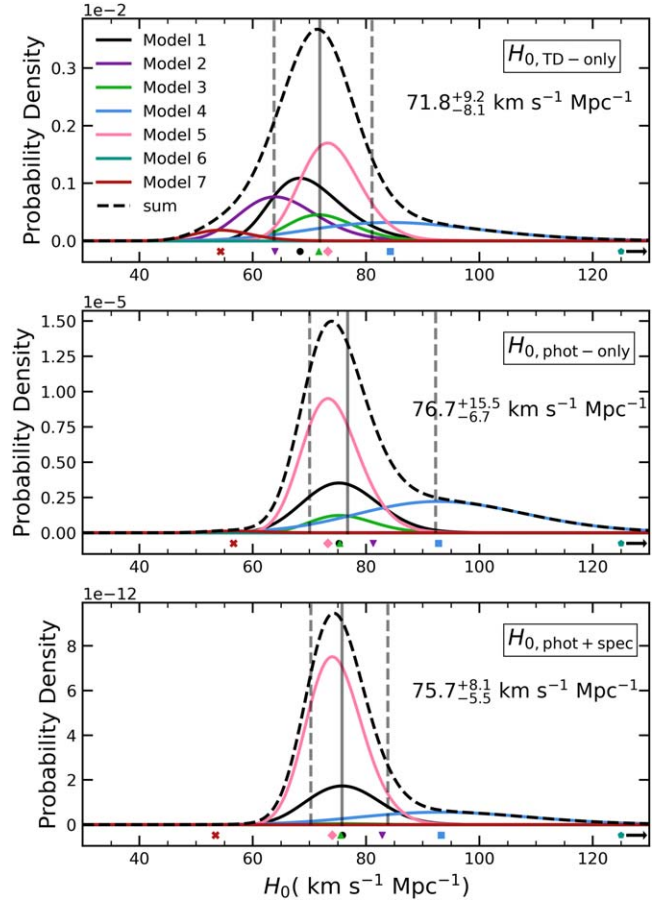
Figure 4. Inferred H_0 from comparing the lens-model-predicted time delays and absolute magnifications to those measured from (in order of increasing constraints) only time delays (top), only photometry (middle), and combined photometry and spectroscopy (bottom). The summed PDF (dashed curves) represents the PDF of H_0 inferred by the total likelihoods of Equations (5) and (7). Individual lens model inferences (solid curves) are shown with normalization equal to their weighting, and the median prediction of each model is plotted as markers below the curves; both the weightings and median H_0 values are given in Table 2. The median of model 6 pushes up to the $H_0 \leqslant 130$ km s^{-1} Mpc^{-1} prior in all cases, and is instead shown with an arrow.

10.1. Time-delay Cosmography With a Type Ia Supernova

SNe Ia as standard candles offer unique advantages for time-delay cosmography compared to SNe II such as ranking the lens models via absolute magnification, constraining the impact of mass-sheet degeneracy, and providing an alternative
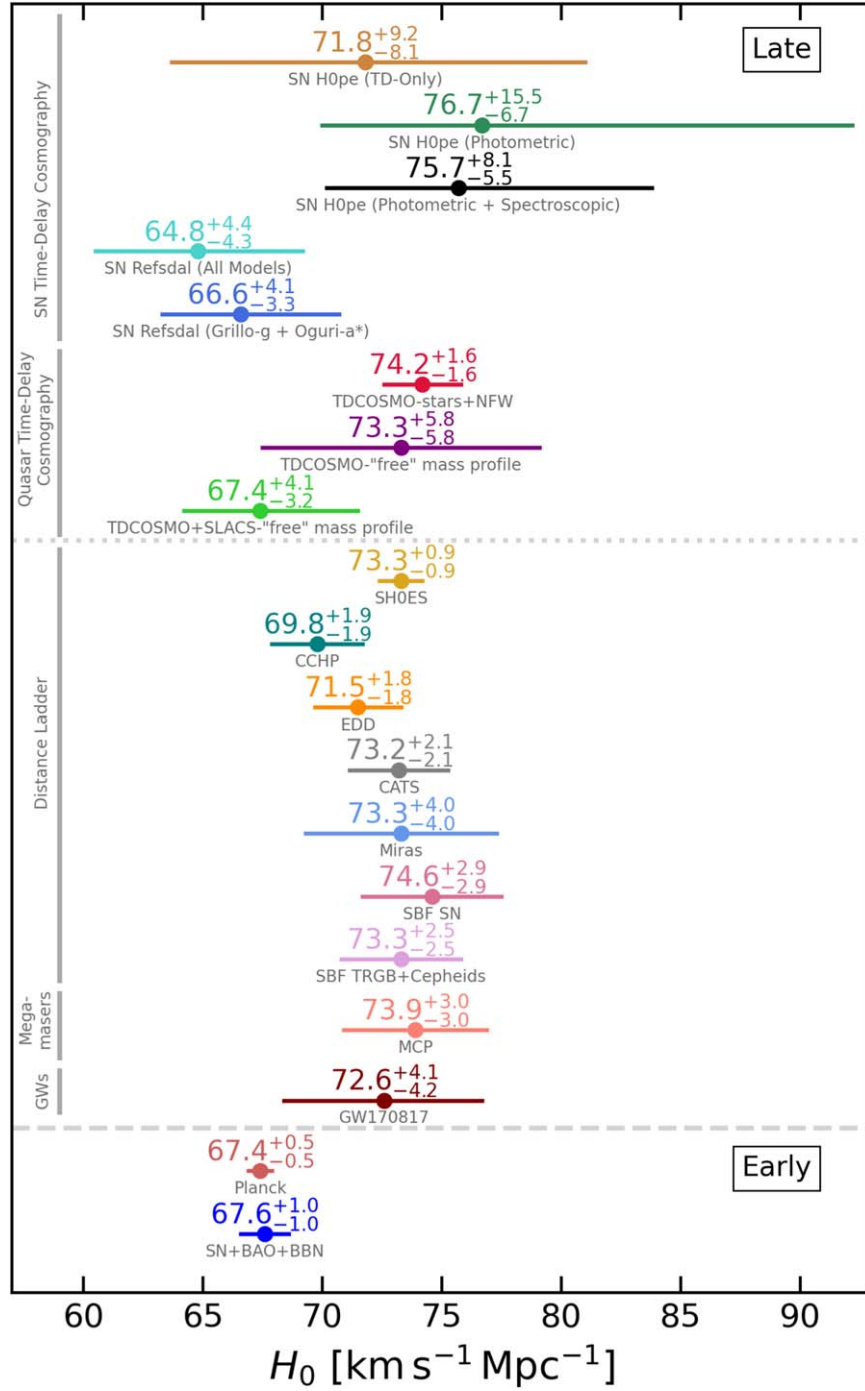
Figure 5. H_0 measurements from SN H0pe compared to other independent methods, broadly divided into late- and early time measurements. SN time-delay cosmography measurements include those from SN Refsdal (P. L. Kelly et al. 2023) using all contributing lens models and using a subset of two models (Grillo-g and Oguri-a*). Quasar time-delay cosmography measurements include those using fully analytic mass profiles (stars + Navarro–Frenk–White (NFW); M. Millon et al. 2020) and free-form mass profiles ("free" mass profile; S. Birrer et al. 2020) from lenses within the TDCOSMO collaboration as well as the Sloan Lens ACS sample (A. S. Bolton et al. 2006). Distance-ladder measurements include those from SH0ES (Y. S. Murakami et al. 2023), the CCHP (W. L. Freedman et al. 2019), the EDD (G. S. Anand et al. 2022), CATs (D. Scolnic et al. 2023), Miras (C. D. Huang et al. 2020), SBF from SNe (P. Garnavich et al. 2023), and TRGBs + Cepheids (J. P. Blakeslee et al. 2021). Measurements using megamasers from the MCP (D. W. Pesce et al. 2020) and using GW170817 as a standard siren (Y.-Y. Wang et al. 2023) are also included. Early time measurements include those from CMB anisotropies from the Planck collaboration (Planck Collaboration et al 2020) and from large-scale-structure clustering using SNe, baryon acoustic oscillation (BAO), and Big Bang nucleosynthesis (BBN) data (N. Schöneberg et al. 2022). This figure is adapted from V. Bonvin & M. Millon (2020).

and independent method to measure the time delays and magnifications via spectroscopy. As a start, we assess the impacts of SN type by repeating the inference of H_0, this time by modifying the set of observables to include only constraints available to SNe II: the photometric measurements

of the time delays and the magnification ratios. This exercise, which makes use of magnification ratios, returns $H_{0,\,\text{Type II}} = 73.0^{+11.3}_{-7.8}$ km s^{-1} Mpc^{-1}, providing no meaningful improvement over the inference from time delays alone, $H_{0,\text{TD-only}}$. This test demonstrates that all the lens models which

satisfy the time-delay ratios also satisfy the measured magnification ratios to within 1σ. While magnification ratios do not give additional footholds to break the degeneracy between the lens models and H_0, absolute magnifications do provide the necessary leverage to rank the lens models. It can be seen that the photometric magnification measurements alone already tighten the overall constraints, downweighting two models which initially satisfied the magnification ratios. On combining the photometric measurements with the spectroscopic measurements, the best constraints of all are obtained, thereby favoring a single lens model (Figure 4). This clearly demonstrates how the magnification helps break this degeneracy and improves the precision of the H_0 inference.

10.2. Lens Model Covariance

The contributing lens models exhibit varying degrees of covariance between the predicted absolute magnifications and the time delays. The likelihoods of Equations (5) and (7) depend on both the time delays and magnifications, implying this covariance affects both the H_0 inference made by each individual lens model as well as their relative weightings. The lens-model-predicted absolute magnifications and time delays are inversely correlated, meaning lower magnifications are associated with larger time delays (2D posteriors in Figure 6) and therefore larger values of H_0. Among the parametric models (1, 2, and 3), this correlation extends between the models, manifesting as an inverse correlation between $H_{0,\text{TD-only}}$ and the predicted magnification of each model. Y. Liu & M. Oguri (2024) found the same correlation for SN Refsdal. The semi- and nonparametric models (4, 5, 6, and 7), however, do not follow this correlation across models, affirming they likely probe a different parameter space than parametric models and one that cannot easily be recreated through variations in the parameterization (e.g., the slope of the radial density profile).

Across the full set of models, the parametric models tended to exhibit a stronger correlation between magnifications and time delays than the nonparametric models, perhaps owing to the inflexibility of fully parameterized mass distributions enforcing a stricter allowable parameter space. We also found that using magnification as a constraint in the lens modeling produces results consistent with the expectations of the covariance (see purple contours of Figure 6). The specifics of these "unblinded" models are detailed in Appendix E.

10.3. The Mass-sheet and Related Degeneracies

Time-delay cosmography can be limited by model-independent degeneracies, such as the mass sheet and by extension mass–slope degeneracies, the latter of which is present in simply parameterized mass models. This implies that the time delays and magnifications are sensitive to the addition of constant sheets of surface mass density or variations in the slope of the radial surface-density profile, both of which may still satisfy the lensing constraints (C. S. Kochanek 2002; P. Schneider & D. Sluse 2013). While these degeneracies tend to plague galaxy–galaxy lenses, in galaxy-cluster lenses they can be broken by the availability of two or more multiple-image systems at different spectroscopically confirmed redshifts (E. E. Falco et al. 1985; Y. Kawano & M. Oguri 2006; P. Schneider & D. Sluse 2014). For example, C. Grillo et al. (2020, 2024) examined the case of SN Refsdal in the MACS J1149 cluster field and concluded that the availability of
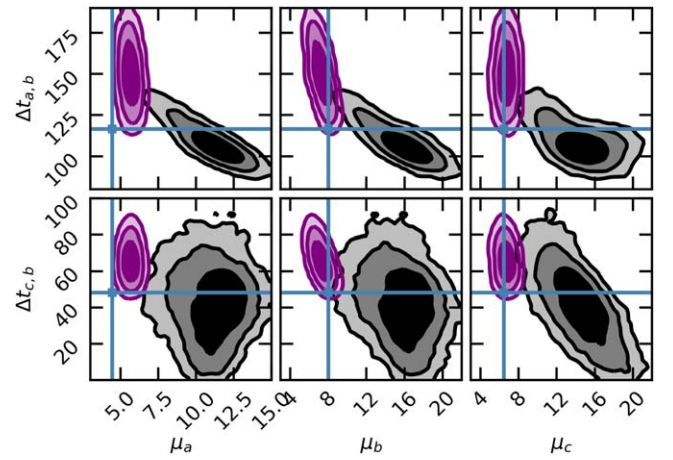

Figure 6. 2D posterior distributions relating time delays and absolute magnifications predicted by the blinded lens model 2 used in this study (black). The contours represent the 68, 95, and 99% confidence intervals, and the measured values from LC fitting are overplotted (blue lines). As seen in the black contours, the blinded lens-model-predicted magnifications and time delays are inversely correlated. We also plot posteriors for a lens model constructed after unblinding which uses an identical approach to model 2, with the exception that the magnifications measured from LC fitting are now applied as constraints in modeling (referred to as an "unblinded" version of the model; purple contours). Including magnification constraints causes the predicted time delays to become larger, following the expectation from the covariance of the blinded model.

89 multiple images from 27 distinct multiple-image systems (eight with unique spectroscopic redshifts) diminished these degeneracies to insignificant levels. However, Y. Liu & M. Oguri (2024) found for a similar set of lensing constraints (but different lens modeling approach) that the mass–slope degeneracy, while diminished, could be still further decreased by the incorporation of new multiple-image systems.

G165 presents five systems at three unique spectroscopically confirmed redshifts and an additional 16 multiple-image systems with photometric constraints. These constraints already break these degeneracies, however it is unlikely that they are completely eliminated, as is illustrated by the scatter in our seven model-predicted time delays. Furthermore, as pointed out in Section 10.1, many of the lens models satisfy the measured magnification ratios yet do not agree with the measured magnification, an indication of the mass-sheet degeneracy at play. This further emphasizes the importance of obtaining a magnification constraint, which has been widely advocated for resolving this degeneracy in galaxy–galaxy and galaxy-cluster lenses alike (e.g., M. Oguri & Y. Kawano 2003; M. Foxley-Marrable et al. 2018; S. Birrer et al. 2022; Y. Liu & M. Oguri 2024).

As discussed in Section 10.1, a magnification constraint is effective at breaking the degeneracy among lens models, reflecting its leverage over the mass-sheet degeneracy. It is interesting to ask to what degree the measured magnification precision can constrain such a mass sheet. The mass-sheet degeneracy, or more generally the mass-sheet transformation allows for a mapping of the surface mass density $\kappa' = \lambda\kappa + (1 - \lambda)$, which induces a change in the true source position $\beta' = \lambda\beta$ while leaving the apparent source position invariant. The second term in the convergence transformation $(1 - \lambda)$, makes up a constant sheet of surface mass density, which gives the mass-sheet transformation its name; we refer to this term as κ_λ. This directly scales the magnifications $\mu' = \mu/\lambda^2$ and time delays $\Delta t' = \lambda\Delta t$, however it is clear the

ratios remain invariant. From photometry and spectroscopy, the magnifications are generally measured to an average fractional precision $\sim 25\%$. This implies that a single magnification measurement can rule out $|\Delta\lambda| \gtrsim 0.1$ or directly $|\kappa_\lambda| \gtrsim 0.1$. When combining all three multiple images, this holds the potential to be much stronger. For example we evaluate lens model 5, which gives the best agreement with measured magnifications, and in postprocessing apply a range of $\lambda \in [0.8, 1.2]$ to its predicted magnifications. We find that only a very small lambda, $\Delta\lambda \sim 0.05$, is required to reduce the model weighting by a factor of 2, implying only a very small allowance of $|\kappa_\lambda| \lesssim 0.05$.

We emphasize this test is not comprehensive: an external convergence need not present itself as a constant sheet of mass (N. Khadka et al. 2024), and it alone does not quantify the extent to which the availability of many multiple-image systems breaks this degeneracy. In the case of an individual lens model, the degeneracy could be quantified explicitly by incorporating free parameters for the addition (or subtraction) of sheets of constant surface mass density or for varying the slope of the surface mass density profile during optimization (e.g., C. Grillo et al. 2020, 2024). This could capture degeneracies between an external convergence and the lens model parameters, which are not addressed in our test. For example, such an external convergence could result in a fundamentally different lens model with a distinct κ distribution (e.g., the isodensity contours are not preserved). Similarly, testing a wide variety of mass profile parameterizations, such as in Y. Liu & M. Oguri (2024), could illustrate the degree of any persisting mass–slope degeneracy. Incorporating magnification constraints into these tests gives additional opportunities to explore lensing degeneracies at the cluster lensing scale, but is outside the scope of this work.

Y. Kawano & M. Oguri (2006) found time-delay ratios can provide an alternate route to breaking the mass–slope degeneracy. This constraint is rarely highlighted in the literature, but its power is apparent in the inference of $H_{0,\text{TD-only}}$ in this study, where the time-delay ratio alone determines the model weighting. This weighting provides an 12% fractional uncertainty in the $H_{0,\text{TD-only}}$ measurement, but removal of this weighting scheme (i.e., the PDFs of the models are rescaled to the same normalization) results in uncertainties which are larger by more than a factor of 2. This demonstrates the utility of multiple-image systems for which multiple precision time delays are available, as these hold an under-recognized ability to break lensing degeneracies.

10.4. Type Ia Supernova Apparent Magnitude Interpolation

To ensure the magnifications for SN H0pe are measured independently of cosmology, both the spectroscopic and photometric methods compared the peak apparent magnitude of each SN image to the distribution of field SNe Ia. Due to the relatively small number of spectroscopically confirmed SNe Ia at $z > 1$ (D. M. Scolnic et al. 2018), the field SN Ia peak magnitudes had to be fit with a smooth model to enable an interpolated inference at $z = 1.783$. Before the unblinding step in this analysis a choice was made to perform this fit with a Gaussian process, but after the unblinding we explored two additional options for the fitting to understand the impact for our measurement. We fit the field SN Ia peak magnitudes with a second-order polynomial in $\log(z)$ space (allowing all coefficients to vary), as well as with a second-order
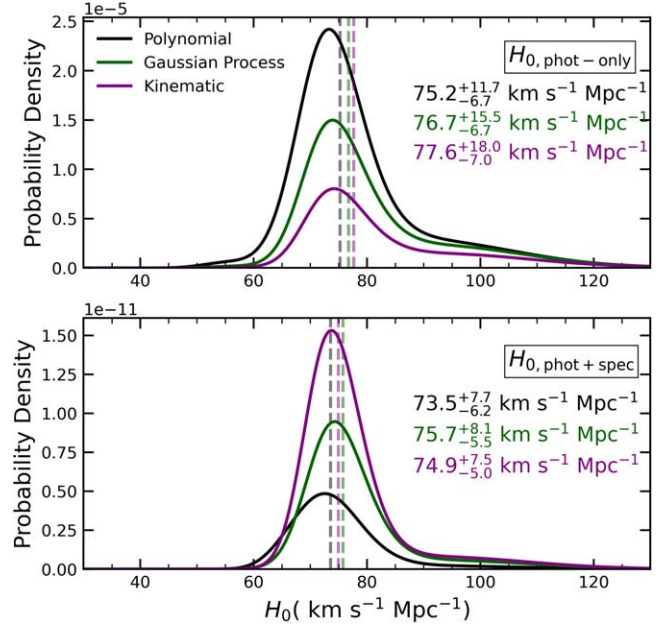

Figure 7. The effect of different interpolation methods for estimating the unlensed SN Ia apparent magnitude at $z = 1.783$ on H_0. We compare the inferred H_0 under three interpolation approaches: polynomial, Gaussian process, and kinematic expansion. The interpolation method affects the inferred magnification of each SN image, which in turn influences the H_0 inference. The impact is ~3% for both photometric-only constraints and joint photometric–spectroscopic constraints, well within the 1σ uncertainties.

cosmology-independent kinematic expansion (see A. G. Riess et al. 2022, Equation (4)).

We find that the range predicted by these three methods is fairly large, ~ 0.3 mag, but that the Gaussian process result is situated directly in the center of the polynomial and kinematic expansion fits (see Figure 6 of J. D. R. Pierel et al. 2024, in preparation). We cannot change this method after unblinding, as there is no evidence to suggest any of the three approaches are in error. Nevertheless we evaluate the impact of the interpolation method on the H_0 inference, as this value directly translates to the magnification measurements and therefore affects the H_0 prediction. The inferences across the three interpolation methods are shown in Figure 7; the median H_0 varies at most 3% in both the photometric and the joint photometric–spectroscopic inferences. As more SNe Ia at $z > 1.5$ are spectroscopically confirmed, the three methods are expected to converge while still remaining independent of cosmology.

10.5. Error Budget

The lens model predictions and the photometric plus spectroscopic measurements both contribute significantly to the error budget, resulting in the $\sim 9\%$ uncertainty in the joint photometric–spectroscopic H_0 inference (Table 2 column 2). Lens model 5 dominates the weighting in this inference and by itself gives $\sim 6.5\%$ uncertainties for H_0 (see the model 5 row of Table 2). The difference between these uncertainties confirms that disagreements among lens models drive up the uncertainty. This represents the systematic uncertainty of the lens models, which could be mitigated by stricter magnification constraints from photometry and spectroscopy or by including new lensing constraints (e.g., Y. Liu & M. Oguri 2024). We found the

removal of image systems which did not have spectroscopic redshifts worsened the agreement between the lens-model-predicted magnifications and observations, demonstrating that even photometrically selected image systems can provide impactful constraints on the lens models. Thus the addition of new photometric systems, or spectroscopic confirmation of existing systems may both serve to increase lens model precision.

The photometric time delays each carry an $\sim 8\%$ uncertainty, but the inclusion of two time delays is more constraining than a single one of similar precision. To estimate the error budget, the two time delays can be approximated as a single effective time delay with uncertainty $\sim 8\%/\sqrt{2} = 5.6\%$ (following error propagation through Equation (3)). Indeed, an H_0 inference assuming zero uncertainty from the lens models (i.e., taking the time delays of lens model 5 with zero error bars) gives an uncertainty on H_0 of 5%–6%, consistent with the expectation from the single effective time delay. Taking this approximation, we can straightforwardly decompose the $\sim 9\%$ H_0 uncertainty into a two-fifths contribution from photometry and spectroscopy and a three-fifths contribution from lens modeling. Furthermore, the lens model uncertainty can be decomposed into a one-fourth "measurement" uncertainty (originating from a single model) and a three-fourths "systematic" uncertainty (the spread between contributing models).

As shown above, ignoring the lens model uncertainty altogether still results in a modest H_0 uncertainty, and therefore improvements in photometry or spectroscopy still matter. Approved follow-up JWST Cycle 3 imaging (PID: 4744) after SN H0pe has faded will provide a template image for precision difference-image photometry, which is expected to improve magnification constraints and nearly halve the photometric time-delay uncertainties. This could result in as small as a 2.8% effective time-delay uncertainty. Given an effective lens model time-delay uncertainty of 7% (which approximately accounts for the model 5 uncertainties and smaller contributions of other lens models), this would translate to an $\sim 7.5\%$ uncertainty on H_0. Should the improved magnification constraints from photometry prove to entirely favor a single lens model, this could push the uncertainty to $\lesssim 5\%$.

11. Conclusions

SN H0pe is only the second opportunity for precision SN time-delay cosmography. We measured the probability distribution of H_0 by comparing the photometrically and spectroscopically measured time delays and magnifications to those predicted by seven independently created lens models, inferring $H_0 = 75.7^{+8.1}_{-5.5} \, \mathrm{km \, s^{-1} \, Mpc^{-1}}$. We found the lens-model-predicted time delays and magnifications were correlated, such that including magnifications could break degeneracies between the lens models and H_0, influencing both the H_0 prediction of each individual lens model as well as weighing its contribution to the total inference. We demonstrated this constraint is a powerful tool to select for lens model accuracy, disfavoring lens model predictions that otherwise would have been admitted had the SN been a Type II. The lens model predictions and combined photometric–spectroscopic measurements both contribute significantly to the error budget, resulting in the $\sim 9\%$ uncertainty in the joint photometric–spectroscopic inference. Follow-up epochs of JWST NIRCam imaging after SN H0pe has faded are approved, and will improve the precision of the SN photometry, and hence also

both the time-delay and magnification estimates. This combined with the additional constraining power provided by two precision time delays may allow for constraints at the $\lesssim 5\%$ level, comparable to or exceeding that of SN Refsdal.

SN H0pe is the first cluster-lensed SN where the methodology for the H_0 inference could be developed in advance of the lens model construction and photometric and spectroscopic measurements. All lens modelers received identical lensing constraints, providing a novel opportunity to ensure consistency between lens models and test lens systematics. We found it was crucial to establish rules for blinding due to the number of independent teams contributing to the analysis, which included a formalized process to address errors. We distinguished objective errors from subjective choices, and only admitted changes to the former following unblinding. These protocols were successfully implemented for SN H0pe and provide a timely point of reference for growing the catalog of H_0 measurements from cluster-lensed SNe. Upcoming surveys from the Vera C. Rubin and Nancy Grace Roman observatories as well as continuing JWST programs will increase the sample of cluster-lensed SNe, which promises to ultimately drive H_0 constraints down to percent-level precision.

Appendix A
The Seven Cluster Lens Models

All models were constructed using the same set of lensing constraints and were blinded from one another as well as from the photometrically and spectroscopically measured time delays and magnifications. The exception is model 5, for which the modelers knew the spectroscopic results but did not include them in the lens model constraints. Model 7 was constructed prior to the unblinding, but was not present at the unblinding owing to logistical difficulties. The model was later added to the analysis. Table A1 gives goodness-of-fit statistics and modeling parameters. The lens models all showcase relatively good quality fits as evidenced by the small rms offsets between the modeled and observed multiple images and the general agreement among the lens models' predictions.

Model 1 implements the GLAFIC software (M. Oguri 2010, 2021), which utilizes a parametric approach to solve for the analytic lens profiles. GLAFIC adopts an adaptive-mesh grid to increase computation efficiency, essentially increasing resolution in regions with larger magnification gradients (e.g., near-critical curves). The model used five NFW profiles to model the dark matter halos of the cluster. These were chosen to correspond to the five bright galaxies which make up the centers of the two merging mass components. The cluster galaxies were modeled with pseudo-Jaffe ellipsoid profiles scaled according to each galaxy's observed F200W flux density. An external shear component was included to improve fitting flexibility. Higher-order multipole perturbations $m = 3$ and 4 (where $m = 2$ represents external shear) were also included. Free parameters were also included for the redshifts of the 16 photometrically constrained multiple-image systems. The optimization was performed using an image-plane χ^2 approximately estimated in the source plane (See M. Oguri 2010 appendix) using an MCMC method with $\sim 10^4$ steps. This approximate χ^2 has been found to well correlate with the true image-plane χ^2 (Figure 5 of M. Oguri 2010).

Model 2 was created using a revised version of the parametric approach detailed by A. Zitrin et al. (2015). The new version (sometimes referred to as Zitrin-Analytic; see also L. J. Furtak et al. 2023) is no longer limited to a grid resolution. This approach operates similarly to other parametric lens modeling techniques and has been successfully applied to JWST imaging of other clusters (e.g., M. Pascale et al. 2022b; A. K. Meena et al. 2023). The model employs two primary components, each described by an analytic profile. The cluster galaxies were parameterized as double pseudoisothermal elliptical mass density distributions (Á. Elìasdóttir et al. 2007) scaled by their luminosities following common relations. The cluster-scale dark matter halo was parameterized with a pseudoisothermal elliptical mass density distribution (PIEMD; A. Kassiola & I. Kovner 1993). Constituting a minor component, the masses of four central galaxies were scaled independently to allow further flexibility ($(\alpha, \delta) =$ (11:27:06.6969, +42:27:50.363), (11:27:20.0475, +42:29:08.292), (11:27:14.4389, +42:28:14.066), and (11:27:14.5094, +42:28:07.004)). While the model can incorporate galaxy ellipticities, for the current model all cluster galaxy profiles were assumed to be circular. In a suite of self-simulated mass distributions, both image- and source-plane optimizations accurately recovered the input parameters, fulfilling the expectation that these should perform similarly (C. R. Keeton 2010). For G165, the model optimization was performed in the source plane via MCMC sampling, which was sampled to derive the uncertainties. The MCMC consisted of ~ 100 initial chains of $\sim 10^3$ steps, which is then refined by a final chain run for $\sim 10^4$ steps. For more details on the methodology, including scaling relations and minimization, we refer to L. J. Furtak et al. (2023).

Model 3 was constructed using LENSTOOL,[18] which applies parametric mass profiles constrained straightforwardly by the observed positions of the multiply imaged systems. In this case, the only mass profiles employed were the $z \approx 0.35$ cluster members identified by B. L. Frye et al. (2024) plus two cluster-scale halo profiles for the dominant components of the merging cluster, all having a PIEMD profile. Positions and shape parameters (ellipticity and orientation) of the cluster members were held fixed to their F200W values. The mass of each cluster member was scaled in proportion to its F200W flux, following M. Limousin et al. (2005). A characteristic $L_\star$ galaxy at the cluster redshift ($m_{\rm F200W} = 17.0$ AB mag) was set to a velocity dispersion $\sigma_0^\star$, a core radius $r_{\rm core}^\star$, and a cutoff radius $r_{\rm cut}^\star$. The core radius was fixed to $r_{\rm core}^\star = 0.15$ kpc similar to other SL works (e.g., T. L. Johnson et al. 2014), while the velocity dispersion and cutoff radii were left to be freely optimized by the model. The masses were fixed according to their scaling relative to $L_\star$ with the exception of the brightest cluster galaxy (BCG) and a perturber cluster galaxy near Arc 3 ($(\alpha, \delta) = (11:27:14.304, +42:28:32.32)$), whose scalings were optimized independently. For the two cluster halos, their positions, ellipticities, orientations, velocity dispersions (mass), and core radii were left free to vary. The halos' cut radii are poorly constrained and therefore were held fixed at 1 Mpc. The redshifts of the 16 photometrically constrained multiple-image systems were left to be freely optimized by the model. This model was optimized in the image plane with a positional uncertainty $\sigma_{\rm pos} = 0\overset{''}{.}3$, which was chosen to match the rms of earlier model iterations. This model was optimized using MCMC sampling, and was run with 10 chains of 1000 steps each, which was found to be much longer than the burn-in time of $\lesssim 100$ steps. For further model information, we refer to P. S. Kamieneski et al. (2024).

The model detailed above was constructed following unblinding, correcting a number of issues in the initial blinded model. The blinded iteration fixed the reference values for the cluster-member scaling relations to a velocity dispersion $\sigma_0^\star = 120$ km s^{-1} and a cutoff radius $r_{\rm cut}^\star = 30$ kpc. While these values were commensurate with findings from other works (e.g., M. Limousin et al. 2008; L. J. Furtak et al. 2023; G. Mahler et al. 2023), it was found to bias the model toward lower magnifications. Leaving these to be freely optimized instead found a much different, but reasonable solution $\sigma_0^\star = 210$ km s^{-1} and $r_{\rm cut}^\star = 8$ kpc.

The blinded iteration of the model was run via source-plane optimization with a small positional uncertainty $\sigma_{\rm pos} = 0\overset{''}{.}03$. While this was chosen to match the astrometric uncertainty of the observed lensed-image centroids (which were independently assigned to the same image pixel by multiple team members), previous works using parametric models indicated that this likely underestimated the uncertainties of the model (A. Zitrin et al. 2015; C. Grillo et al. 2016). The source-plane approach, which approximated an image-plane chi-squared (see Equation (12) of E. Jullo & J. P. Kneib 2009), was found to

---

[18] https://projets.lam.fr/projects/lenstool/wiki

Table A1
Lens Model Information

#	Model and Reference	rms (″)	$\sigma_{pos,SN}$ (″)	$\sigma_{pos,global}$ (″)	DOF	χ_ν	Optimization
1	GLAFIC (M. Oguri 2010, 2021)	0.07	0.1	0.1	119	0.44	Source
2	Zitrin-analytic (A. Zitrin et al. 2015)	0.21	0.1	0.3[a]	86	0.61	Source
3[b]	LENSTOOL (J.-P. Kneib et al. 2011)	0.16	0.3	0.3	109	0.3	Image
4	MARS (S. Cha & M. J. Jee 2022)	0.07	N/A	N/A	N/A	N/A	Source
5	W. Chen et al. (2020)	0.1	0.18[c]	0.18[c]	N/A	N/A	Image
6	WSLAP+ (J. M. Diego et al. 2005)	1.1	0.03	0.03	N/A	N/A	Image
7	Zitrin-LTM (A. Zitrin et al. 2009)	0.7	0.1	0.5[a]	95	1.23	Image

Notes. Columns are the rms separation between the model and observed positions lensed images (rms), the positional uncertainty for multiple-image systems used for the χ^2 minimization ($\sigma_{pos,global}$), the positional uncertainty used for the SN images ($\sigma_{pos,SN}$), the number of degrees of freedom (DOF) in the model, the χ^2 per DOF (χ_ν^2), and which plane the minimization was performed in ("Optimization"). All quantities are given for the best-fit model. rms and σ_{pos} refer to the image plane unless otherwise specified. "N/A" indicates quantities that are not applicable to nonparametric models, for which chi-squared statistics are not relevant for parameter estimation.

[a] Uncertainties are extracted using an effective positional uncertainty $\sigma_{pos,global} \sim 1.4$ following the prescription of A. Zitrin et al. (2015).

[b] This model was updated following unblinding, the blinded version of the model was run with source-plane optimization using a positional uncertainty 0.03, resulting in an rms of 0.26 and $\chi_\nu^2 = 72$. This blinded model is detailed in this appendix.

[c] Effective positional uncertainty approximated for reference; model is not optimized using chi-squared statistics.

also underperform the image-plane optimization, producing an rms nearly a factor of 2 larger, and suffered from unphysical solutions at the larger positional uncertainty. The source-plane model also showed evidence for being generally less robust: for example, the posterior median was found to change with positional uncertainty (which was not seen in the image-plane variant). For these reasons, the corrected model was run in the image plane, which may have implications for the model posteriors (see Appendix C). The results of the blinded model are noted in Table 1, and the impact of its correction on the H_0 inference is detailed in Section 8.

Model 4 was constructed by the MARS algorithm (S. Cha & M. J. Jee 2022), which is a free-form, grid-based approach. MARS consists of two terms, one a chi-square minimization of SL multiple images in the source plane and the other a regularization term. The MARS algorithm adopts maximum cross entropy for the regularization. This approach can suppress fluctuations and generate a quasi-unique solution for a given SL multiple images. For lens modeling, MARS can consider not only SL multiple images but also WL galaxies (S. Cha et al. 2024). To account for WL galaxies, MARS utilizes an additional term that minimizes differences between observed and predicted reduced shear. For this study, MARS provided lens models from both SL-galaxy-only and SL + WL data sets to predict magnifications and time delays. The SL-galaxy-only model consists of a 100×100 pixel grid covering $90'' \times 90''$ around the two BCGs. The SL + WL model consists of a 400×400 pixel grid encompassing the entire $360'' \times 360''$ field of view. One of the interesting differences between the SL-only and the SL + WL reconstructed mass distributions is that the SL-only model shows an offset of the mass peak from the northeastern core because of the deficiency of SL multiple images, but the SL + WL mass map exhibits good agreement with the luminosity distributions of the galaxy-cluster members.

Model 5 uses the lens modeling software originally developed for a blind prediction of the SN Refsdal reappearance and time delays (W. Chen et al. 2020). This approach makes minimal assumptions about the mass distribution at the galaxy-cluster scale, similar to nonparametric methods, but uses a parametric approach at the individual-galaxy scale. This semiparametric method parameterizes the dark matter halos of the cluster galaxies as symmetric analytic NFW profiles (J. F. Navarro et al. 1997) with the same scale radius and assumes the halo mass scales in proportion to stellar flux. The scale radius is set to 3.84 kpc, and the mass–luminosity ratio for $r < 30$ kpc, M/L ($r < 30$ kpc) $= 9.4$ $M_\odot/L_\odot$. The luminosity is measured from JWST F090W photometry (approximately V/R band rest frame). The goal of the cluster-member halos is to serve as an initial condition of a concentrated mass distribution around the core of each cluster member, as this cannot be well constrained by observed multiple images due to the cluster-scale lensing. These profiles do not hold after many iterations of the global perturbation function described below, such that the final solution of the cluster-scale mass distribution is only weakly dependent on the choice of scale radius and halo mass. For the cluster-scale dark matter distribution, the model makes no assumptions about symmetry. Instead, the global lensing potential is deformed by a set of curving functions that apply numerical perturbations to the potential. These curving functions are inherently smooth on the cluster scale and are applied to determine a source-plane position that minimizes the separation between the source-plane positions of lensed multiple images of image families. The model aims to find the best source-plane position for each set of multiple images that can minimize the image-plane offset. Thus, although the perturbations are driven by the source-plane positions, the model is still optimized using image-plane statistics. While the only previous application of this model was to the MACS J1149.5+2223 cluster, its predictions of the reappearance position of SN Refsdal's image SX as well as SN Refsdal's four relative time delays and magnification ratios are consistent with other well-tested parametric models (P. L. Kelly et al. 2023). This model does not optimize for the redshifts of photometrically constrained multiple-image systems, but instead these systems are assigned to their photometric redshifts and are given a factor of 2.5 lower weighting in the model optimization compared to systems with spectroscopic redshifts.

Model 6 is a hybrid model, implementing the WSLAP+ (J. M. Diego et al. 2005) software, where the large-scale component of the lens model is described by a grid of

Gaussians, and the small-scale component traces the light distribution of member galaxies. The model is optimized by solving a system of two linear equations per lensing constraint (one for the x-coordinate and one for the y-coordinate) of the form $\theta = \beta - \alpha(\theta, M)$ with θ the observed position of the lensed galaxy, β the unknown position of the galaxy in the source plane, and $\alpha(\theta, M)$ the deflection angle at the position θ produced by the unknown mass distribution M.

For G165, the distribution of grid points for the smooth component was built recursively with a first solution obtained from a uniform grid that was then used to derive an adaptive grid that increased the spatial resolution in regions with higher mass concentrations. Using the adaptive grid, WSLAP+ derived 20 solutions varying the initial guess from the optimization and the redshifts of the systems with photometric redshifts. These models were used to derive predicted magnifications and time delays at the three model-predicted positions of SN H0pe. The lack of lensing constraints in the east portion of the cluster and between the two groups resulted in large variations in the predicted magnifications and time delays. In particular, the critical curve at $z = 1.78$ exhibits a dual behavior with some models predicting a single critical curve that connects both groups and other models predicting two disjoint critical curves, one around each group. Model 6 is the only lens model which predicts image C of the SN to arrive last, which is inconsistent with measurements from both photometric LC fitting and spectroscopic age dating. This results in the model receiving zero weighting across all three H_0 inferences, as each make use of time-delay ratio constraints. Across the suite of solutions used to derive the model uncertainties, some solutions do correctly predict the image arrival order, indicating that new lensing constraints may improve the accuracy of the model.

Model 7 uses an updated version of the Zitrin-LTM software (A. Zitrin et al. 2009, A. Zitrin et al. 2015; see also T. Broadhurst et al. 2005), which was modified to accommodate time-delay cosmography of galaxy-cluster lenses following SN Refsdal (see A. Zitrin 2020). In this semiparametric approach, it is assumed that the light traces the mass (LTM), such that observed cluster-member light is assumed to trace the underlying dark matter. The stellar mass of each cluster galaxy is represented analytically as a power-law mass–surface-density profile with relative weights determined by the galaxy F200W brightness. The profiles are then simultaneously smoothed with a Gaussian kernel to approximate the projected cluster-scale dark matter distribution, which receives a free weighting relative to the parametric galaxy component. An external shear component with free amplitude and position angle is also applied to broadly account for systematics like large-scale structure. Finally, additional flexibility is included for individual galaxies of interest, which included two nearby perturber galaxies specified in Section 6, and the three brightest central galaxies. For the bright galaxies, the position angle, ellipticity, and mass-to-light ratio can be fit freely. Five of the image systems were set to their spectroscopic redshifts, and for all other systems the redshifts were left free in the model, using the photometric redshift estimate of B. L. Frye et al. (2024) as an initial guess. The minimization of the model is done in the image plane, using an MCMC method with a final chain of 2000 steps from which the posteriors are sampled.

Appendix B
Lens Model Positional Uncertainties

The positional uncertainties of the lens models play a determining role in the time-delay and magnification errors of the parametric lens models of this sample, namely models 1, 2, 3, and 7. The choice of positional uncertainty is not straightforward. It is suggested that, in order to correctly capture lensing systematics (e.g., line-of-sight structure or complex structure within the cluster), it should be chosen to be large enough that the rms of each model is comparable to the positional uncertainties assigned to the multiple-image systems, and the resulting χ_ν^2 values are near unity (e.g., A. Zitrin et al. 2015; C. Grillo et al. 2016). We stress that this metric is not always a useful guideline (for example, it is not a relevant metric for nonparametric models), and that the choice of positional uncertainty is not agreed upon across lens models in the literature (e.g., M. Meneghetti et al. 2017; P. L. Kelly et al. 2023). There is also not a consensus whether this guideline is best suited for the case of a single cluster (e.g., A. Acebron et al. 2022), whether it should be chosen based off the results of many clusters (e.g., A. Zitrin et al. 2015), or drawn from results of simulated clusters (A. D'Aloisio & P. Natarajan 2011; E. Jullo et al. 2010). As seen in Table A.1, all but one lens model (for which chi-squared statistics are applicable) satisfy or exceed these guidelines, implying these models adequately capture or even overestimate their uncertainties. One exception, lens model 3, did show large discrepancies between its rms and positional uncertainty and by extension a large χ_ν^2, which warranted further investigation and updating of the choice of positional uncertainty as detailed in Appendix A. We note that the posteriors of models 2 and 7 are sampled with an effective positional uncertainty of $\sigma_{\rm pos} \sim 1\overset{''}{.}4$, such that their reduced chi-squared values become much lower than 1, however this positional uncertainty was found to best account for systematics across a range of clusters (A. Zitrin et al. 2015).

We emphasize that the choice of positional uncertainty was left to the expertise of each individual lens modeling team. In a landscape where the choice of positional uncertainty is not agreed upon, we favor this approach, and a discussion of appropriate positional uncertainties is outside the scope of this work. However it is interesting to ask how standardizing the models by their positional uncertainty or chi-squared statistics would affect the H_0 inference. For this exercise, we approximate the posterior of each lens model as a single multivariate Gaussian (this results in only minor information loss since the posteriors are fairly well-behaved), and, assuming a Gaussian likelihood, can approximate the effect of increasing or decreasing the positional uncertainty on the lens model time-delay and magnification PDFs as scaling the PDF width linearly with the positional uncertainty (i.e., scaling with $\sqrt{\chi_\nu^2}$).

This was not straightforward for each model; here we detail the modifications made to each model posterior to achieve this standard. For model 1, the posterior width is rescaled by a factor of $\sqrt{0.44}$ to achieve an effective chi-squared of unity, narrowing the uncertainties by $\sim$33%. For lens models 2 and 7, the effective positional uncertainty used to generate the posteriors ($\sigma_{\rm pos} = 1\overset{''}{.}4$) was already chosen to have $\chi_\nu^2 \sim 1$ across a large sample of lensing clusters, and as such these are left unchanged. We note that the reduced chi-squared is already

far below unity assuming $\sigma_{\mathrm{pos}} = 1\overset{''}{.}4$, and rescaling the posterior width would result in much smaller uncertainties on the time delays and magnifications. For model 3, which had $\chi^2_\nu = 0.30$, the uncertainties are rescaled by a factor $\sqrt{0.30}$. In the case of model 5, positional uncertainties and chi-squared statistics are not applicable; instead an effective positional uncertainty is estimated as $\sigma = 0\overset{''}{.}18$ and the posterior widths are rescaled by $0.1/0.18 = 0.56$ to match the positional uncertainty to the rms of $0\overset{''}{.}1$ (this is similar to achieving a reduce chi-squared of unity when assuming a Gaussian likelihood, as seen in model 1). Models 4 and 6 are left unchanged: model 4 does not make use of positional uncertainty (a term for the mean source scatter is used in uncertainty estimation, however it is not functionally equivalent the positional uncertainty term of typical parametric lens models; see S. Cha & M. J. Jee 2022; S. Cha et al. 2024), and model 6's uncertainties are determined via modification of the lensing assumptions, not the positional uncertainty.

Performing this test and recomputing the H_0 inference results in only very minor changes: $H_{0,\mathrm{TD-only}} = 72.9^{+9.9}_{-8.0}$, $H_{0,\mathrm{phot-only}} = 75.3^{+16.6}_{-5.3}$, $H_{0,\mathrm{phot+spec}} = 74.9^{+6.5}_{-4.7}$ km s^{-1} Mpc^{-1}. As is apparent, none of the inferences are affected in a statistically significant fashion, despite most of the lens models having a substantial reduction in their uncertainties. This follows the expectation of Section 10.5, where the uncertainty of the individual lens model is subdominant to the uncertainty induced by the spread between lens models.

While the results of this exercise are to be taken with caution, as there is no straightforward way to standardize the diverse set of lens models on the basis of positional uncertainty or chi-squared statistics, it further emphasizes the findings of Section 10.5. The precision of the magnification and time-delay ratio measurements from photometry and spectroscopy are such that they can find agreement with multiple lens models, however these lens models can exhibit $\gtrsim 1\sigma$ tensions between one another. In this regime, the disagreement between lens models is the dominant barrier in reducing the uncertainty on H_0, highlighting the importance of using a range of models to capture lensing systematics. This in turn implies that the uncertainty estimation for any individual lens model is likely sufficient for this inference, but as time-delay and magnification measurements improve (thereby improving the weighting scheme) or as the agreement between lens models improve (e.g., refining multiple-image systems, using magnifications or time-delay ratios as model constraints), the uncertainties of individual lens models will ultimately have the greatest impact on the H_0 uncertainty.

Appendix C
The Plane of Optimization

This analysis includes lens models which optimize both in the image plane and in the source plane (see Table A1). Both approaches have been shown to perform similarly in previous analyses on galaxy-cluster lenses (e.g., M. Meneghetti et al. 2017), however this has not been thoroughly evaluated for time delays in the literature. More generally, for this precise measurement, it is useful to evaluate the effects of the plane of optimization. Across the seven lens models in the sample, no clear trend emerges upon comparison of the source-plane and image-plane models, however the approaches of these models are in some cases substantially different. To better quantify this effect, we investigate models 1, 2, and 3, which had the

functionality to optimize in the image plane and the source plane (however we note that this functionality is not typically used in the literature for models 1 and 2). Model 4 cannot be optimized in the image plane, however this effect is likely subdominant to the the regularization term used in its minimization (see S. Cha & M. J. Jee 2022).

Each image-plane model was run using the same constraints as its source-plane counterpart, and the resultant magnifications and time delays were compared. For Models 1 and 2, the source- and image-plane models were found to agree at the $<1\sigma$ level; this corroborates findings from previous testing of these software on simulated lenses (L. J. Furtak et al. 2023; M. Oguri 2010). By contrast the model 3 source-plane model was found to produce larger magnifications by $\sim10\%$ while inferring similar time delays. In principle, the use of the magnification tensor in the source-plane chi-squared should prevent such an effect, preventing models from arbitrarily scaling the magnification to minimize the scatter of images in the source plane (e.g., M. Oguri 2010). One caveat is that source-plane models may find unphysical solutions, predicting counterimages which are not observed, however upon inspection this does not occur in model 3. We speculate that the software model 3 uses, LENSTOOL, may struggle with posterior estimation with the source-plane χ^2. E. Jullo et al. (2007) caution this software may be less robust with this approach. Indeed in testing we found the source-plane optimization to behave in unreliable ways (e.g., the choice of positional uncertainty affected the posterior medians) whereas the image-plane optimization did not. Furthermore providing the image-plane model solution to the source-plane χ^2 yielded a better solution than what was found in the source-plane optimization.

Across the three models, this may tentatively suggest that overall source-plane optimization is a sufficient approximation for the current lens model precision. However we caution that for this cannot be taken for granted, and some models show significant deviations in their solutions between the source and image plane. As lensing constraints grow tighter (e.g., more spectroscopic redshifts and more image systems), image-plane modeling may be preferred, and further detailed comparison between these approaches is needed in future work.

Appendix D
Probability Distribution Function Parameterization and Likelihood Integration

The PDFs from the photometric LC fitting, spectroscopic fitting, and the lens model fitting are parameterized as Gaussian mixture models (GMMs). Each fit (photometry, spectroscopy, or lens model), F, generated a few hundred to thousands of samples from the posterior distribution, $P(\mathcal{O}|F)$, which was then fit by a linear combination of N multivariate Gaussians such that:

$$P(\mathcal{O}|F) \approx \sum_{i=1}^{N} w_i \mathcal{N}_F(\mathcal{O}|\mu_i, \mathcal{C}_i), \qquad (\mathrm{D1})$$

where w_i is the weight assigned to each normalized multivariate Gaussian, μ_i and $\mathcal{C}_i$ are the associated mean vectors and covariance matrices, respectively, and N was chosen for each model based on the Bayesian information criterion to avoid overfitting to artifacts which may result from undersampling. Thus, the integrand in Equation (5) becomes the product of two

GMMs or equivalently the sum of products of multivariate Gaussians:

$$
\int P(\mathcal{O}|M_l; H_0) P(\mathcal{O}|LC) d\mathcal{O}_1...d\mathcal{O}_n
$$
$$
= \int \sum_{i=1}^{N} \sum_{j=1}^{N} w_i w_j \mathcal{N}_{M_l}(\mathcal{O}|\mu_i, \mathcal{C}_i) \mathcal{N}_{LC}(\mathcal{O}|\mu_j, \mathcal{C}_j) d\mathcal{O}_1...d\mathcal{O}_n,
$$
(D2)

where i indices refer to the Gaussians which make up the GMM representing the lens model posterior, and the j indices refer to the Gaussians which make up the GMM representing the LC fitting posterior. This formalism is advantageous in that this integral can be solved analytically as the multiplication of two multivariate Gaussians is itself a multivariate Gaussian with a known renormalization.

The combined photometric–spectroscopic likelihood of Equation (7) follows the same formalism, where the posterior from spectroscopic fitting is also parameterized as a GMM, and the integrand is the distributive product of three GMMs. Because the product of any two multivariate Gaussians is itself a Gaussian, the product of three multivariate Gaussians is also a Gaussian.

Appendix E
Unblinded Lens Models

After the submission of the blinded model results, the contributing lens model teams also had the option to construct unblinded lens models, where absolute magnifications measured from LC fitting were used as constraints. Only the teams for models 2 and 4 did so, but these two models represent both parametric and nonparametric types. Figure 6 illustrates parameter changes and their covariance for model 2. Reassuringly, the unblinded model 2 posterior follows the expectations from the correlations seen in the blinded model posterior, where the median predicted time delay increases due to the now-lower magnifications. The nonparametric model 4, however, saw very little change in its time-delay predictions. The blinded version of model 4 predicts fairly accurate magnifications with the exception of μ_a, but μ_a is the only magnification which lacks significant covariance between the time delays, resulting in only minor changes to the time delays in the unblinded model.

For both unblinded models, we infer only $H_{0,\text{TD-only}}$ because the magnifications became constraints in the lens models rather than predicted observables. While model 4 gives similar results in both the blinded and unblinded cases, the unblinded model 2 gives a much larger H_0 than the blinded model. Interestingly, both unblinded models predict the time-delay ratio more accurately than their blinded counterparts, implying they would receive generally higher weighting in the $H_{0,\text{TD-only}}$ inference. While it is difficult to make strong conclusions based on a sample of only two models, it is interesting to ask whether unblinding the magnifications may better address systematics between lens models, allowing for more modeling approaches to accurately reproduce the observables and hence contribute to the H_0 inference. As the sample of cluster-lensed SNe Ia grows, functionality for magnification constraints will likely become more ubiquitous in lens modeling techniques, creating an opportunity for a more comprehensive view of lens model systematics.

Appendix F
Testing Lens Model Systematics

All seven lens models were fully blinded from the time delays, magnification ratios, and absolute magnifications inferred from the photometric LC fitting of J. D. R. Pierel et al. (2024, in preparation). While these measurements provide strong constraining power for weighting model contributions to H_0, they also introduced an opportunity to test lens model systematics using the absolute magnification at the galaxy-cluster scale with a multiply imaged source. Note that this is a more stringent test than lower-magnification singly imaged cases such as SN HFF14Tom in the A2744 cluster field (S. A. Rodney et al. 2016). Here we broadly follow S. A. Rodney et al. (2016) to provide an in-depth discussion of the performance of the contributing models, which in turn determines the weighted contributions to the H_0 measurement.
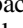
Parametric versus nonparametric. While the contributing models are broadly divided into two categories, parametric and nonparametric, each model is distinct from one another. Here we compare the most free-form models, models 4 and 6, to the three classically parametric models, models 1, 2, and 3.

We find the nonparametric models have longer relative time delays (assuming the fiducial H_0 value), and hence higher H_0 inferences than the parametric models. The inferred H_0 values also have higher uncertainties. This may be owing to the greater flexibility of nonparametric models, which can explore solutions for the lens potential inaccessible to rigid fully parametric profiles. Owing to the lack of sufficient lensing constraints about the northeastern core of the cluster, parametric methods do effectively reduce the parameter space by assuming the analytic profiles are centered at the locations of the BCGs. As shown in Table 2, both parametric and nonparametric models receive significant weighting under all three inferences, where the weighting reflects the agreement between model predictions of observables and their corresponding measurements from photometry and spectroscopy. As the nonparametric models tended to predict longer time delays, this emphasizes the need for a wide variety of lens model approaches to fully capture the range of possible solutions.

Strong versus strong + weak. Model 4 makes use of both WL and SL constraints. While only this model was used for the H_0 inference, an additional version of the model using only SL was also constructed for testing purposes only. This comparison offers a rare opportunity to evaluate the benefits of WL. The addition of WL constraints are found to generally increase the time-delay uncertainties without greatly impacting their median, while decreasing the uncertainties on the magnifications and generally shifting their median lower. This significantly improves the agreement of both the lens-model-predicted time-delay ratios and the predicted magnifications with those measured by photometry and spectroscopy. As a result, the model receives a much greater weighting in the $H_{0,\text{phot + spec}}$ inference, increasing the weighting to 14% for strong + weak constraints rather than <1% for SL alone. This suggests that WL constraints are crucial for nonparametric modeling methods, especially when the available number of SL constraints is low.

ORCID iDs

Massimo Pascale ⓘ https://orcid.org/0000-0002-2282-8795
Brenda L. Frye ⓘ https://orcid.org/0000-0003-1625-8009
Justin D. R. Pierel ⓘ https://orcid.org/0000-0002-2361-7201

Wenlei Chen https://orcid.org/0000-0003-1060-0723
Patrick L. Kelly https://orcid.org/0000-0003-3142-997X
Seth H. Cohen https://orcid.org/0000-0003-3329-1337
Rogier A. Windhorst https://orcid.org/0000-0001-8156-6281
Adam G. Riess https://orcid.org/0000-0002-6124-1196
Patrick S. Kamieneski https://orcid.org/0000-0001-9394-6732
José M. Diego https://orcid.org/0000-0001-9065-3926
Ashish K. Meena https://orcid.org/0000-0002-7876-4321
Sangjun Cha https://orcid.org/0000-0001-7148-6915
Masamune Oguri https://orcid.org/0000-0003-3484-399X
Adi Zitrin https://orcid.org/0000-0002-0350-4488
M. James Jee https://orcid.org/0000-0002-5751-3697
Nicholas Foo https://orcid.org/0000-0002-7460-8460
Reagen Leimbach https://orcid.org/0009-0001-7446-2350
Anton M. Koekemoer https://orcid.org/0000-0002-6610-2048
C. J. Conselice https://orcid.org/0000-0003-1949-7638
Liang Dai https://orcid.org/0000-0003-2091-8946
Ariel Goobar https://orcid.org/0000-0002-4163-4996
Matthew R. Siebert https://orcid.org/0000-0003-2445-3891
Lou Strolger https://orcid.org/0000-0002-7756-4440
S. P. Willner https://orcid.org/0000-0002-9895-5758

References

Acebron, A., Grillo, C., Bergamini, P., et al. 2022, ApJ, 926, 86
Anand, G. S., Tully, R. B., Rizzi, L., Riess, A. G., & Yuan, W. 2022, ApJ, 932, 15
Birrer, S., Amara, A., & Refregier, A. 2016, JCAP, 2016, 020
Birrer, S., Dhawan, S., & Shajib, A. J. 2022, ApJ, 924, 2
Birrer, S., Shajib, A. J., Galan, A., et al. 2020, A&A, 643, A165
Blakeslee, J. P., Jensen, J. B., Ma, C.-P., Milne, P. A., & Greene, J. E. 2021, ApJ, 911, 65
Blandford, R., & Narayan, R. 1986, ApJ, 310, 568
Bolton, A. S., Burles, S., Koopmans, L. V. E., Treu, T., & Moustakas, L. A. 2006, ApJ, 638, 703
Bonvin, V., & Millon, M. 2020, H0LiCOW H0 Tension Plotting Notebook, v1.0, Zenodo, doi:10.5281/zenodo.3635517
Bonvin, V., Courbin, F., Suyu, S. H., et al. 2017, MNRAS, 465, 4914
Bradač, M., Schneider, P., Lombardi, M., & Erben, T. 2005, A&A, 437, 39
Broadhurst, T., Benìtez, N., Coe, D., et al. 2005, ApJ, 621, 53
Cha, S., HyeongHan, K., Scofield, Z. P., Joo, H., & Jee, M. J. 2024, ApJ, 961, 186
Cha, S., & Jee, M. J. 2022, ApJ, 931, 127
Chen, W., Kelly, P. L., & Williams, L. L. R. 2020, RNAAS, 4, 215
Chen, W., Kelly, P. L., Oguri, M., et al. 2022, Natur, 611, 256
Dai, L., Kaurov, A. A., Sharon, K., et al. 2020, MNRAS, 495, 3192
Dalal, N., Hennawi, J. F., & Bode, P. 2005, ApJ, 622, 99
D'Aloisio, A., & Natarajan, P. 2011, MNRAS, 411, 1628
Dhawan, S., Johansson, J., Goobar, A., et al. 2020, MNRAS, 2639, 491
Diego, J. M., Protopapas, P., Sandvik, H. B., & Tegmark, M. 2005, MNRAS, 360, 477
Diego, J. M., Broadhurst, T., Chen, C., et al. 2016, MNRAS, 456, 356
Elìasdóttir, Á., Limousin, M., Richard, J., et al. 2007, arXiv:0710.5636
Falco, E. E., Gorenstein, M. V., & Shapiro, I. I. 1985, ApJL, 289, L1
Foxley-Marrable, M., Collett, T. E., Vernardos, G., Goldstein, D. A., & Bacon, D. 2018, MNRAS, 478, 5081
Freedman, W. L., Madore, B. F., Hatt, D., et al. 2019, ApJ, 882, 34
Frye, B., Pascale, M., Qin, Y., et al. 2019, ApJ, 871, 51
Frye, B., Pascale, M., Cohen, S., et al. 2023, TNSAN, 96, 1
Frye, B. L., Pascale, M., Pierel, J., et al. 2024, ApJ, 961, 171
Furtak, L. J., Zitrin, A., Weaver, J. R., et al. 2023, MNRAS, 523, 4568
Garnavich, P., Wood, C. M., Milne, P., et al. 2023, ApJ, 953, 35
Gilman, D., Birrer, S., & Treu, T. 2020, A&A, 642, A194
Gladders, M. D., & Yee, H. K. C. 2000, AJ, 120, 2148
Goobar, A., Amanullah, R., Kulkarni, S. R., et al. 2017, Sci, 356, 291
Goobar, A., Johansson, J., Schulze, S., et al. 2023, NatAs, 7, 1098
Grayling, M., Thorp, S., Mandel, K. S., et al. 2024, MNRAS, 531, 953
Grillo, C., Pagano, L., Rosati, P., & Suyu, S. H. 2024, A&A, 684, L23
Grillo, C., Rosati, P., Suyu, S. H., et al. 2020, ApJ, 898, 87
Grillo, C., Karman, W., Suyu, S. H., et al. 2016, ApJ, 822, 78
Grillo, C., Rosati, P., Suyu, S. H., et al. 2018, ApJ, 860, 94
Halkola, A., Seitz, S., & Pannella, M. 2006, MNRAS, 372, 1425
Hoekstra, H., Franx, M., & Kuijken, K. 2000, ApJ, 532, 88
Hsiao, E. Y., Conley, A., Howell, D. A., et al. 2007, ApJ, 663, 1187
Huang, C. D., Riess, A. G., Yuan, W., et al. 2020, ApJ, 889, 5
Jee, M. J., White, R. L., Ford, H. C., et al. 2006, ApJ, 642, 720
Johnson, T. L., Sharon, K., Bayliss, M. B., et al. 2014, ApJ, 797, 48
Jullo, E., & Kneib, J. P. 2009, MNRAS, 395, 1319
Jullo, E., Kneib, J. P., Limousin, M., et al. 2007, NJP, 9, 447
Jullo, E., Natarajan, P., Kneib, J. P., et al. 2010, Sci, 329, 924
Kaiser, N., & Squires, G. 1993, ApJ, 404, 441
Kamieneski, P. S., Frye, B. L., Windhorst, R. A., et al. 2024, ApJ, 973, 25
Kassiola, A., & Kovner, I. 1993, ApJ, 417, 450
Kawano, Y., & Oguri, M. 2006, PASJ, 58, 271
Keeton, C. R. 2001, arXiv:astro-ph/0102340
Keeton, C. R. 2010, GReGr, 42, 2151
Kelly, P. L., Rodney, S. A., Treu, T., et al. 2015, Sci, 347, 1123
Kelly, P. L., Rodney, S. A., Treu, T., et al. 2016, ApJL, 819, L8
Kelly, P. L., Rodney, S., Treu, T., et al. 2023, Sci, 380, abh1322
Khadka, N., Birrer, S., Leauthaud, A., & Nix, H. 2024, MNRAS, 533, 795
Kneib, J.-P., Bonnet, H., Golse, G., et al., 2011 LENSTOOL: A Gravitational Lensing Software for Modeling Mass Distribution of Galaxies and Clusters (Strong and Weak Regime), Astrophysics Source Code Library, ascl:1102.004
Kochanek, C. S. 2002, ApJ, 578, 25
Kolatt, T. S., & Bartelmann, M. 1998, MNRAS, 296, 763
Limousin, M., Kneib, J.-P., & Natarajan, P. 2005, MNRAS, 356, 309
Limousin, M., Richard, J., Kneib, J. P., et al. 2008, A&A, 489, 23
Liu, Y., & Oguri, M. 2024, arXiv:2402.13476
Mahler, G., Jauzac, M., Richard, J., et al. 2023, ApJ, 945, 49
Mandel, K. S., Thorp, S., Narayan, G., Friedman, A. S., & Avelino, A. 2022, MNRAS, 510, 3939
McCully, C., Keeton, C. R., Wong, K. C., & Zabludoff, A. I. 2014, MNRAS, 443, 3631
Meena, A. K., Zitrin, A., Jiménez-Teja, Y., et al. 2023, ApJL, 944, L6
Meneghetti, M., Natarajan, P., Coe, D., et al. 2017, MNRAS, 472, 3177
Millon, M., Galan, A., Courbin, F., et al. 2020, A&A, 639, A101
Murakami, Y. S., Riess, A. G., Stahl, B. E., et al. 2023, JCAP, 2023, 046
Navarro, J. F., Frenk, C. S., & White, S. D. M. 1997, ApJ, 490, 493
Oguri, M. 2010, PASJ, 62, 1017
Oguri, M. 2015, MNRAS, 449, L86
Oguri, M. 2021, PASP, 133, 074504
Oguri, M., & Kawano, Y. 2003, MNRAS, 338
Pascale, M., Frye, B. L., Dai, L., et al. 2022a, ApJ, 932, 85
Pascale, M., Frye, B. L., Diego, J., et al. 2022b, ApJL, 938, L6
Pesce, D. W., Braatz, J. A., Reid, M. J., et al. 2020, ApJL, 891, L1
Pierel, J. D. R., Rodney, S., Vernardos, G., et al. 2021, ApJ, 908, 190
Pierel, J. D. R., Arendse, N., Ertl, S., et al. 2023, ApJ, 948, 115
Pierel, J. D. R., Newman, A. B., Dhawan, S., et al. 2024, ApJL, 967, L37
Planck Collaboration, Aghanim, N., Akrami, Y., et al. 2020, A&A, 641, A6
Polletta, M., Nonino, M., Frye, B., et al. 2023, A&A, 675, L4
Ponente, P. P., & Diego, J. M. 2011, A&A, 535, A119
Raney, C. A., Keeton, C. R., & Brennan, S. 2020, MNRAS, 492, 503
Refsdal, S. 1964, MNRAS, 128, 307
Riess, A. G., Yuan, W., Macri, L. M., et al. 2022, ApJL, 934, L7
Rodney, S. A., Brammer, G. B., Pierel, J. D. R., et al. 2021, NatAs, 5, 1118
Rodney, S. A., Strolger, L. G., Kelly, P. L., et al. 2016, ApJ, 820, 50
Sawicki, M. 2002, AJ, 124, 3050
Schneider, P. 1985, A&A, 143, 413
Schneider, P., Ehlers, J., & Falco, E. E. 1992, Gravitational Lenses (Berlin: Springer)
Schneider, P., & Sluse, D. 2013, A&A, 559, A37
Schneider, P., & Sluse, D. 2014, A&A, 564, A103
Schöneberg, N., Verde, L., Gil-Marìn, H., & Brieden, S. 2022, JCAP, 2022, 039
Scolnic, D., Riess, A. G., Wu, J., et al. 2023, ApJL, 954, L31
Scolnic, D. M., Jones, D. O., Rest, A., et al. 2018, ApJ, 859, 101
Sendra, I., Diego, J. M., Broadhurst, T., & Lazkoz, R. 2014, MNRAS, 437, 2642
Shajib, A. J., Mozumdar, P., Chen, G. C. F., et al. 2023, A&A, 673, A9
Sharon, K., & Johnson, T. L. 2015, ApJL, 800, L26
Suyu, S. H., Goobar, A., Collett, T., More, A., & Vernardos, G. 2024, SSRv, 220, 13
Suyu, S. H., & Halkola, A. 2010, A&A, 524, A94
Treu, T., Brammer, G., Diego, J. M., et al. 2016, ApJ, 817, 60
Vega-Ferrero, J., Diego, J. M., Miranda, V., & Bernstein, G. M. 2018, ApJL, 853, L31
Verde, L., Schöneberg, N., & Gil-Marìn, H. 2024, ARA&A, 62, 287

Wang, Y.-Y., Tang, S.-P., Jin, Z.-P., & Fan, Y.-Z. 2023, ApJ, 943, 13
Windhorst, R. A., Cohen, S. H., Jansen, R. A., et al. 2023, AJ, 165, 13
Wong, K. C., Keeton, C. R., Williams, K. A., Momcheva, I. G., &
    Zabludoff, A. I. 2011, ApJ, 726, 84

Wong, K. C., Suyu, S. H., Chen, G. C. F., et al. 2020, MNRAS, 498, 1420
Zitrin, A. 2020, arXiv:2008.10641
Zitrin, A., Broadhurst, T., Umetsu, K., et al. 2009, MNRAS, 396, 1985
Zitrin, A., Fabris, A., Merten, J., et al. 2015, ApJ, 801, 44